NASA/TM–1998-112236

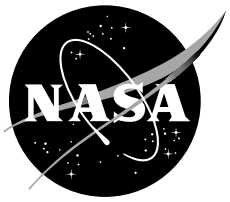

CFD Modelling of Bore Erosion in Two-Stage Light Gas Guns

D. W. Bogdanoff

August 1998

The NASA STI Program Office . . . in Profile

Since its founding, NASA has been dedicated to the advancement of aeronautics and space science. The NASA Scientific and Technical Information (STI) Program Office plays a key part in helping NASA maintain this important role.

The NASA STI Program Office is operated by Langley Research Center, the Lead Center for NASA's scientific and technical information. The NASA STI Program Office provides access to the NASA STI Database, the largest collection of aeronautical and space science STI in the world. The Program Office is also NASA's institutional mechanism for disseminating the results of its research and development activities. These results are published by NASA in the NASA STI Report Series, which includes the following report types:

- TECHNICAL PUBLICATION. Reports of completed research or a major significant phase of research that present the results of NASA programs and include extensive data or theoretical analysis. Includes compilations of significant scientific and technical data and information deemed to be of continuing reference value. NASA's counterpart of peer-reviewed formal professional papers but has less stringent limitations on manuscript length and extent of graphic presentations.

- TECHNICAL MEMORANDUM. Scientific and technical findings that are preliminary or of specialized interest, e.g., quick release reports, working papers, and bibliographies that contain minimal annotation. Does not contain extensive analysis.

- CONTRACTOR REPORT. Scientific and technical findings by NASA-sponsored contractors and grantees.

- CONFERENCE PUBLICATION. Collected papers from scientific and technical conferences, symposia, seminars, or other meetings sponsored or cosponsored by NASA.

- SPECIAL PUBLICATION. Scientific, technical, or historical information from NASA programs, projects, and missions, often concerned with subjects having substantial public interest.

- TECHNICAL TRANSLATION. English-language translations of foreign scientific and technical material pertinent to NASA's mission.

Specialized services that complement the STI Program Office's diverse offerings include creating custom thesauri, building customized databases, organizing and publishing research results . . . even providing videos.

For more information about the NASA STI Program Office, see the following:

- Access the NASA STI Program Home Page at *http://www.sti.nasa.gov*

- E-mail your question via the Internet to help@sti.nasa.gov

- Fax your question to the NASA Access Help Desk at (301) 621-0134

- Telephone the NASA Access Help Desk at (301) 621-0390

- Write to:
  NASA Access Help Desk
  NASA Center for AeroSpace Information
  7121 Standard Drive
  Hanover, MD 21076-1320

NASA/TM–1998-112236

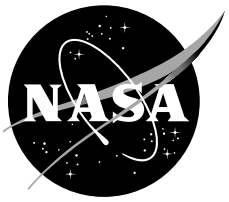

CFD Modelling of Bore Erosion in Two-Stage Light Gas Guns

D. W. Bogdanoff
Thermosciences Institute
Ames Research Center, Moffett Field, California

National Aeronautics and
Space Administration

Ames Research Center
Moffett Field, California 94035-1000

August 1998

Acknowledgments

The author would like to acknowledge the excellent work of the range engineer, Charles J. Cornelison, and the gun crew, Donald M. Holt and Donald B. Bowling. Support by NASA (Contract NAS-2-14031) to Eloret is gratefully acknowledged.

Available from:

NASA Center for AeroSpace Information
7121 Standard Drive
Hanover, MD 21076-1320
(301) 621-0390

National Technical Information Service
5285 Port Royal Road
Springfield, VA 22161
(703) 487-4650

CFD Modelling of Bore Erosion in Two-Stage Light Gas Guns

D. W. BOGDANOFF

Thermosciences Institute
Ames Research Center

Abstract

A well-validated quasi-one-dimensional computational fluid dynamics (CFD) code for the analysis of the internal ballistics of two-stage light gas guns is modified to explicitly calculate the ablation of steel from the gun bore and the incorporation of the ablated wall material into the hydrogen working gas. The modified code is used to model 45 shots made with the NASA Ames 0.5" light gas gun over an extremely wide variety of gun operating conditions. Good agreement is found between the experimental and theoretical piston velocities (maximum errors of ±2% to ±6%) and maximum powder pressures (maximum errors of ±10% with good igniters). Overall, the agreement between the experimental and numerically calculated gun erosion values (within a factor of 2) was judged to be reasonably good, considering the complexity of the processes modelled. Experimental muzzle velocities agree very well (maximum errors of 0.5–0.7 km/sec) with theoretical muzzle velocities calculated with loading of the hydrogen gas with the ablated barrel wall material. Comparison of results for pump tube volumes of 100%, 60% and 40% of an initial benchmark value show that, at the higher muzzle velocities, operation at 40% pump tube volume produces much lower hydrogen loading and gun erosion and substantially lower maximum pressures in the gun. Large muzzle velocity gains (2.4–5.4 km/sec) are predicted upon driving the gun harder (that is, upon using higher powder loads and/or lower hydrogen fill pressures) when hydrogen loading is neglected; much smaller muzzle velocity gains (1.1–2.2 km/sec) are predicted when hydrogen loading is taken into account. These smaller predicted velocity gains agree well with those achieved in practice. CFD snapshots of the hydrogen mass fraction, density and pressure of the in-bore medium are presented for a very erosive shot.

I. Introduction

A representative two-stage light gas gun is shown (not to scale) in figure 1. The operation of such a gun starts with the burning of the powder in the powder chamber. The piston, typically an easily deformable plastic such as polyethylene, is accelerated in the pump tube to velocities of the order of 0.8 km/sec. The hydrogen in front of the piston is greatly compressed and heated by the piston, reaching pressures on the order of 7000 bar and temperatures that are ideally as high as 3000 K. At some point in the compression cycle, the diaphragm just behind the projectile breaks and the projectile starts to accelerate down the barrel. The highly compressed and heated hydrogen between the piston and the projectile can have a sound speed of ~4 km/sec and can accelerate the projectile to velocities of 7–8 km/sec. With very light projectiles and by driving the gun hard (that is, by using large powder loads and/or low hydrogen fill pressures), velocities up to 11 km/sec can be obtained. Further discussion of the two-stage light gas gun is given in reference 1.

Gun barrel erosion is a serious problem with two-stage light gas guns. Erosion can be caused by thermal, chemical and mechanical factors. Possible erosion modes include thermally induced softening, phase changes and melting of the barrel bore surface. The extreme temperature changes and pressures during gun firing can cause cracking and spalling of the bore surface. The mechanical sweeping action of the gas, as well as the motion of the projectile, can remove liquid or weakened solid material from the bore surface. Chemical factors are more important in conventional guns, where the gunpowder gas contains large quantities of carbon and nitrogen compounds, than in two-stage gas guns. Further discussion of gun erosion is given in references 1 and 2.

Excessive barrel erosion can lead to damage or destruction of the launch package. It can also lead to frequent barrel changes and excessive down-time, especially at higher launch velocities. Barrel erosion can also limit the maximum muzzle velocity by loading down the hydrogen working gas with heavy eroded barrel material (ref. 3). (For brevity, we will use the term “hydrogen loading” to refer to this effect in the remainder of this paper.) One way of attempting to mitigate this problem is to perform a series of CFD calculations at various gun operating conditions and then to make an optimization of the gun operating conditions. Optimizations can be performed on some or all of the following parameters: powder mass, piston mass, projectile mass,

initial hydrogen fill pressure, diaphragm rupture pressure, pump tube volume and contraction cone angle. Such CFD analyses were performed in references 4–8. The analyses can be used to attempt to maximize muzzle velocity, minimize the maximum projectile base pressure for a given muzzle velocity, reduce the maximum strength of the shock waves impacting on the projectile base, etc., as well as to reduce gun barrel erosion. Conditions judged from the calculations to be likely to result in reduced gun erosion can then be tested in actual gun firings. The guidance provided by the numerical CFD calculations greatly reduces the number of actual firings required to find the desired gun operating conditions. [This reduction can be as great as from tens of shots (when no CFD guidance is used) to as few as one or two shots.] This procedure was used in earlier work on the 1.5" and 0.5" guns at the NASA Ames Research Center (refs. 6–8). In these three studies muzzle velocity increases of 0.5–0.8 km/sec were achieved simultaneously with reductions in barrel erosion of 30–50%.

Gun barrel erosion was not explicitly calculated in the CFD calculations of references 4–8, but rough estimates could be made from the calculated values of hydrogen temperature, pressure, velocity and the duration of the erosive conditions. The present report presents an extension of previous work in which the barrel erosion is explicitly calculated and the resulting interaction of the eroded material and the hydrogen working gas is modelled. An equation-of-state is developed for the resulting hydrogen/steel mixture. Standard CFD methods are used to convect this mixture down the barrel. To obtain the erosion rate of the barrel wall, the unsteady heat conduction into the barrel wall is solved concurrently with the flow of the powder gas-piston-hydrogen media within the barrel. The temperature dependence of the conductivity and the specific heat and the phase changes in the gun steel are modelled. A latent heat of fusion is applied at the melting wall surface. Mass flux and heat flux at the wall surface are matched between the in-bore media and the steel parts of the solution. The effects of wall blowing on the skin friction and heat transfer are modelled.

In section II, we first very briefly review (and reference) the previously developed CFD light gas gun code. We then describe, in some detail, the additions made to the code to model wall erosion and the incorporation of the eroded wall material into the hydrogen working gas. Comparisons of the CFD results with analytical solutions are made. In section III, CFD results are compared with experimental piston velocity, powder pressure, muzzle velocity and gun erosion data. The experimental data were taken with three different pump tube volumes and include a number of very high velocity launches (up to 9.5 km/sec). The substantial loss of muzzle velocity due to the loading of the hydrogen working gas by the eroded wall material is clearly demonstrated by the experimental and numerical results. Agreement between the CFD calculations which included incorporation of the eroded wall material into the working gas and the experimental data was found to be very good. The results were much superior and of much broader applicability than those obtained in reference 8 using a simple heuristic correction factor to model the effect of hydrogen loading on muzzle velocity.

II. Numerical Method

A. Original code

The starting point for the CFD code presented herein is an earlier quasi-one-dimensional CFD code first described in reference 9. The code models the entire gun firing cycle from gunpowder ignition to the moment that the projectile exits the muzzle. The code is based on the Godunov method in one dimension and is third-order accurate in space and second-order accurate in time. The Riemann solver used is exact for shocks and uses a very accurate power law integration for expansion waves. Realistic equations-of-state are used for all media. The code includes modelling of friction and heat transfer for powder gas, hydrogen, the pump tube piston and the projectile. A simple nonequilibrium turbulence model is included for the gas flows, and the predictions of skin friction and heat transfer to the tube walls in the gas flows are modified accordingly. Gunpowder burn in the first-stage breech is modelled using standard ballistic techniques.

In reference 9, validation of the code is discussed in some detail. Part of the validation consisted of comparing CFD results with analytical solutions of

(a) Riemann’s shock tube problem.

(b) A solid state plate slap problem.

(c) Flow through a convergent-divergent nozzle with a 300:1 pressure ratio.

(d) Gunpowder burn in a closed chamber.

Further validation of the code was obtained by comparing CFD predictions against experimental data from the Ames 0.5" and 1.5" two-stage light gas guns. The experimental data included

(a) Powder burn pressure histories.

(b) Pump tube pressure histories.

(c) Piston velocities.

(d) Projectile muzzle velocities.

Further details of these validation studies and the code in general are found in reference 9.

B. Code Modifications

Properties of gun steel– To perform the required calculations, it is necessary to obtain the thermal conductivity, specific heat and density of the barrel material (gun steel or carbon steel). Guns are frequently made of the steel alloys 4330 or 4340 (ref. 10). The chemistry of these steels is given in reference 11 and therein it is seen that this chemistry is very similar to the chemistries of alloys 4130 and 4140. Since it was not possible to find a complete set of properties for 4330 steel, properties for the other alloys are used to construct data curves for the gun barrels. The properties do not vary greatly amongst different carbon steel alloys, and hence, the errors produced by using property data from the different alloys are small. Thermal conductivity data for 4130, 4140, 4340 and "1.5% carbon steel" are taken from references 12–14. The temperature range of the data is 123–1473 K. Consensus thermal conductivity data are selected, favoring 4340 steel where the data are available (123–813 K). In lieu of specific data, the thermal conductivity was assumed to be constant from 1473 K up to the melting point.

Specific heat data for 4130 and 4140 steel over the temperature range 348–1048 K are taken from reference 12. Specific heat data for "low Ni" and "high Ni" carbon steels with chemistries close to those of 4330 and 4340 steel are taken from reference 15. The temperature range of these data is 348–1523 K. Again, consensus data are taken to construct the data curve. For want of data, the specific heat is assumed to be constant from 1523 K up to the melting point. The selected specific heat data contain the peaks corresponding to the various phase changes of steel as the temperature is increased. These specific heat data are integrated to provide a curve of internal energy versus temperature for use in the CFD code. The melting point of the steel is taken as 1723 K, from reference 10. The heat of fusion of the steel was taken as 2.8932×10^9 erg/g, from reference 16.

The thermal conductivity and specific heat data are used in the heat conduction calculations in the gun barrel. For these calculations, the density of the barrel is assumed to be constant at 7.80 g/cm^3. The large mass of unheated gun barrel material outside the very thin heated region will restrain the latter in the axial and circumferential directions. The barrel material will expand in the radial direction during heating. This expansion is ignored in the barrel heat conduction calculation in order to avoid calculating a complex stress state in the barrel material near the bore and having the cells move on account of this expansion. This large simplification of the calculations should produce only very minor errors in the erosion calculations.

For the equation-of-state calculations with fine steel droplets (or frozen droplets, i.e., dust) incorporated into the hydrogen working gas, some modifications of the material properties discussed above are used. First, thermal conductivity data are unnecessary, since the steel and the hydrogen are always assumed to be at the same temperature. The steel droplets may melt and/or freeze in the hydrogen-steel flow in the gun barrel and it would be very awkward to calculate the melting or freezing for every cell for every timestep. Hence, for the internal energy versus temperature curve for the steel droplets, the internal energy change due to melting or freezing is assumed to be uniformly distributed over the temperature interval 1700–1750 K, which includes the melting point of 1723 K. For lack of data, the specific heat of the liquid is taken to be equal to the specific heat value of the solid at the highest temperature for which the latter is available. Since the specific heat of the steel is of the order of 0.07 times that of the hydrogen gas, even at fairly heavy mass loadings of the hydrogen with steel, the errors produced by the aforementioned assumptions used to generate the curve of internal energy versus temperature for the steel droplets will introduce only very minor errors in the overall CFD calculations.

The density of the solid or liquid steel was permitted to vary for the droplets incorporated into the hydrogen gas. Density data for solid iron was taken from reference 17. The density of molten iron just above the melting point was taken from reference 18. From these data, a curve of density versus temperature for the steel of the gun barrel was constructed. (Note that the data are actually for iron; the differences between the densities of iron and the carbon steel gun steels are very small.) The abrupt density changes for the phase changes and melting were again taken to be spread out over the 50 K interval containing the temperature of the phase change. The linear expansion coefficient of molten steel was assumed to be the same as that of solid steel at the highest temperature for which such data are available. Since the volume occupied by the steel droplets, even at 50% mass loadings at maximum pressures, is of the order of 1% of the total volume, the small errors in the density of the steel produced by the assumptions made above are unimportant.

For use in the equation-of-state of the hydrogen-steel mixture, the internal energies and densities of the steel

were taken to be functions of temperature only. The variations of these properties with pressure were examined and were found to reach maxima of about 1% for the maximum pressures in the gun. Since the fractions of total internal energy and fluid volume due to that steel are themselves small, the changes of the steel internal energy and density with pressure were ignored, thereby much simplifying the equation-of-state calculations which must be done at every cell at every timestep. The errors produced by these assumptions were estimated to be, at most, 0.1%.

Equation-of-state of hydrogen-steel mixture– The following equations are used for the hydrogen-steel mixture.

$$e = m_1 e_1 + m_2 e_2 \tag{1}$$

and

$$\rho = \frac{1}{\frac{m_1}{\rho_1} + \frac{m_2}{\rho_2}} \tag{2}$$

where

e = internal energy of mixture

e_1 = internal energy of hydrogen

e_2 = internal energy of steel

ρ = density of mixture

ρ_1 = density of hydrogen

ρ_2 = density of steel

m_1 = mass fraction of hydrogen

m_2 = mass fraction of steel

If m_2 is less than 0.0001, we ignore the steel in the flow and simply use the usual tabulated equation-of-state (EOS), $p = p(\rho,e)$ and $T = T(\rho,e)$ for hydrogen, where p is the pressure and T is the temperature. This situation exists for the vast majority of the CFD solutions for the gun firing cycle, and since the two-phase EOS is rather costly in CPU time to employ, it is essential not to use it except when it is absolutely required.

If it is required to use the two-phase EOS, we proceed as follows. From the CFD update to the cell in question, we will know e, ρ, m_1 and m_2, but not e_1, e_2, ρ_1 and ρ_2. For the first iteration, we assume $e_2 = e_1/15.1$, based on an average value of the ratio of specific heats of hydrogen and steel and take $\rho_2 = 6.90$ g/cm^3, the value for liquid steel at 1900 K. With these assumptions, we can then solve equations (1) and (2) for e_1 and ρ_1 and, using the normal EOS for hydrogen, determine p and T. With an estimate for T now available, using the curves established as described in the previous section we can get better estimates for e_2 and ρ_2, and then, using equations (1) and (2) and the EOS for hydrogen alone, a new set of values for p and T can be calculated. Using well-known iterative procedures, the process is then repeated until the p and T values converge adequately.

The speed of sound (c) of the hydrogen-steel mixture is also required in the CFD solution. To calculate c, one considers the motion of the hydrogen-steel mixture along an isentrope with variations of pressure and density. The simplest case is to ignore heat transfer between the hydrogen and the steel. In this case, it can be shown that the speed of sound for the mixture is given by

$$c^2 = c_1^2 \frac{\rho_1^2}{\rho^2 m_1} \tag{3}$$

where c_1 is the speed of sound of the hydrogen gas alone, available from the normal EOS for hydrogen. The primary effect of the steel loading is to reduce the sound speed below the value for hydrogen alone by the factor $\sqrt{m_1}$. If we allow the temperature of the hydrogen and steel to move together along the isentrope, we will get a slightly different expression for c. To make this calculation we again use the assumption that the specific heat of steel is 1/15.1 (= K) times that of hydrogen. In this case, the sound speed for the mixture can be shown to be given by

$$c^2 = \left[c_1^2 + \left.\frac{dp}{de_1}\right|_{\rho_1} \frac{p}{\rho_1^2} Q \right] \frac{\rho_1^2}{\rho^2} \frac{1}{m_1} \tag{4}$$

where

$$Q = -\frac{1}{1 + \frac{m_1}{K(1-m_1)}} \tag{5}$$

The derivative in equation (4) is available from the normal EOS for hydrogen alone. The difference between the sound speeds from equations (3) and (4) is of the order of 1% for $m_1 = 0.5$ and 5% for $m_1 = 0.1$. The CFD solutions are remarkably insensitive to the exact value of c used, and representative gun solutions carried out with the two different ways of calculating c showed only very small differences. Our final choice was to use equation (4) for c. The difference in the CPU times is negligible because most of the time is spent in the iteration procedure described earlier.

Heat conduction analysis in barrel– The basic heat conduction equation used to update the internal energies at the cell centers is given below.

$$\Delta e_i = \frac{\left[\left(k\frac{\partial T}{\partial y}\right)_{i+1/2} - \left(k\frac{\partial T}{\partial y}\right)_{i-1/2}\right]\Delta t}{\rho \Delta y_i} \qquad (6)$$

where

y	=	radial distance away from the bore
i	=	cell identifying index, increasing in the radial direction
i – 1/2, i + 1/2	=	identifying indices of the inner and outer cell boundaries
Δy_i	=	cell thickness in radial direction
Δe_i	=	change in internal energy of the cell
T	=	temperature
k	=	thermal conductivity
ρ	=	density
Δt	=	timestep

The actual problem is axisymmetric, but a planar one-dimensional analysis is used for simplicity because the total thickness of the heat conduction zone analyzed is about 1/15th of the tube radius and the thickness within which significant gradients occur is 3 to 5 times smaller still. Thus, the errors produced by using the planar assumption should be quite small, of the order of 1–2% or less. The derivative terms give the conductive heat flux on the two boundaries of the cell. The format of equation (6) is used for all cells except the innermost cell, where the heat flux at the bore is given by calculations performed in the medium inside the bore of the gun. (These calculations will be described in the next section.) The variations of the steel properties with temperature are taken into account by the variation of k with temperature and the shape of the curve e = e(T), constructed as described earlier. As described earlier, ρ is taken to be a constant within the gun barrel. Equation (6) is solved for each cell for each timestep of the solution.

The stability requirement for the timestep based on the heat conduction calculations in the barrel is taken from reference 19, but we use the notation of the present report and consider the cell with the smallest radial thickness. The result is

$$\Delta t_{max} = \frac{(\Delta y_{min})^2 \rho C}{2k} \qquad (7)$$

where

Δt_{max}	=	maximum permissible timestep
Δy_{min}	=	thickness of cell of smallest radial thickness
C	=	specific heat of steel

We use the smallest value of C in the temperature range of interest to calculate Δt_{max} in equation (7). The actual timestep chosen for each step is the smaller of the timestep calculated based on the CFD calculations for the media within the barrel and 0.75 times the value given in equation (7). The factor of 0.75 provides an extra margin of safety regarding stability of the heat conduction calculations.

We now give some key numerical values for the heat conduction analyses of the NASA Ames 0.5" light gas gun, for which theoretical and experimental results will be given at a later point. The overall gun length is 2019 cm. The grid was 200 cells in the axial direction and 16 cells in the radial direction. The cell length in the axial direction varied from 83 cm in the first-stage powder breech, where heat conduction effects were unimportant, to about 0.5 cm near the diaphragm, where heat transfer and barrel erosion were severe, then increasing to 15 cm at the muzzle. The pump tube and launch tube diameters are 6.45 and 1.27 cm, respectively. The thickness of the innermost cell is 0.00117 cm and, going outwards, each cell is 1.1 times as thick as the preceding cell. The total radial thickness of the zone in which the heat conduction is analyzed is 0.042 cm. In our calculations, the temperature rise of the outermost two or three cells is negligible, so using an adiabatic boundary condition at a depth of 0.042 cm into the barrel causes negligible errors. These numbers have proven to give high quality results for the Ames 0.5" gun. They would very likely have to be changed for guns of different sizes or with much different durations of the launch cycle.

The basic variable for the update of the cell center values using equation (6) is the internal energy, not the temperature. In an earlier version of the cell update routine, the two relations e = e(T) and T = T(e) were used successively. This caused small, but continuously accumulating, errors. Hence, we shifted to using e only in the update of the cell center values. The T = T(e) relation is used to calculate cell center temperatures, which are then used to calculate the temperatures and temperature gradients at the cell boundaries. These are necessary to compute the heat fluxes and are calculated using cubic interpolations to the cell center temperatures. After calculating the cell boundary heat fluxes, these temperatures are discarded and the relation e = e(T) is never used, except once at the very beginning of the run, to set the initial e values for all cells. The accumulating errors mentioned earlier do not

occur with the present analysis technique. The wall temperature is calculated using a quadratic extrapolation from the first three cell center temperatures. This temperature cannot be discarded, because it must be used to couple the steel heat conduction solution with the solution for the medium within the barrel. However, it is never used to make an e = e(T) calculation for the steel.

As heat continues to flow into the barrel from the bore, the barrel temperature will, in general, continue to rise. As long as the barrel surface temperature does not exceed the steel melting temperature, it is assumed that there is no loss of barrel material. On the other hand, when, at the end of a timestep, the barrel surface temperature is calculated to have exceeded the steel melting temperature, barrel material will have been lost during the timestep. The amount of the material lost is calculated, starting with the following equation.

$$\rho\Delta y_1\left(e_1 - e_{10}\right) + \rho\Delta y_M H_f = \left(Q_w - Q_{12}\right)\Delta t \qquad (8)$$

where

Δy_1 = thickness of first cell adjacent to bore

Δy_M = thickness of material lost due to melting

e_{10} = internal energy of first cell at start of timestep

e_1 = internal energy of first cell at end of timestep

H_f = heat of fusion of steel

Q_W = heat flux rate into first cell from medium within bore

Q_{12} = heat flux rate out of first cell into second cell

Other variables are as described previously. Equation (8) has been derived using a control volume approach for the innermost steel cell in the barrel. The first term in equation (8) represents the increase in internal energy of the steel in the cell due to heating. The second term is the energy absorbed due to the melting off of a layer of steel of thickness Δy_M. The term on the right-hand side of the equation represents the difference between the heat gained from the medium in the barrel bore and the heat lost by conduction to the second cell. At the end of the timestep, all terms in equation (8) are known except Δy_M and e_1. By calculating an average specific heat of the steel, C, for the temperature range in question, and rearranging equation (8) to solve for Δy_M, we get

$$\Delta y_M = \frac{\left(Q_W - Q_{12}\right)\Delta t}{\rho H_f} - \frac{\Delta y_1 C\left(T_1 - T_{10}\right)}{H_f} \qquad (9)$$

where

T_{10} = temperature of first cell at start of timestep

T_1 = temperature of first cell at end of timestep

All terms in equation (9) are known except Δy_M and T_1. To solve for Δy_M and T_1, a second equation is needed. This is obtained by making a quadratic extrapolation of temperature from the cell temperatures T_1, T_2 and T_3 to the unknown (new) wall position and setting this temperature equal to the melting temperature, T_M. T_1, T_2 and T_3 are the cell center temperatures after the timestep and the values of T_2 and T_3 are taken to be those after the usual internal cell conduction calculations and are therefore known. This second equation also, then, has the unknowns Δy_M and T_1, and the two equations are solved together by iteration to give the wall retreat, Δy_M, during the timestep. After the calculation of Δy_M, the cell gridding is displaced outwards by this amount. New e values at the cell centers are calculated using quadratic interpolations from the e values at the cell centers at the end of the conduction calculations for the timestep, but before the displacement of the grid.

The numerical solution technique was tested with a constant heat flux applied to the wall and constant steel properties. This ultimately yields a steady-state solution for which an analytical result is available. With a wall temperature of 1200 K, an initial barrel temperature of 300 K, Δy_1 = 0.000875 cm and the ratio of successive cell thicknesses increasing by 1.07 as one moves outwards into the barrel material, the numerical and analytical results were compared. The temperatures were found to have maximum errors of 1–2 K and the numerical wall retreat rate had an error of approximately 0.5%. Similar accuracies were found comparing analytical and numerical results for a simple conduction solution with constant bore surface temperature. The actual value of Δy_1 (0.00117 cm) and the ratio of successive cell thicknesses (1.10) used for our gun calculations are slightly larger than those quoted just above. This should result in errors perhaps two to three times larger than those just quoted. This was judged to be sufficiently accurate for our purposes and the slightly larger cell thicknesses afford a significant reduction in CPU time.

If the wall erosion rate is extremely high, it is possible that the calculated temperature, not only at the barrel wall surface but also at the center of the first steel cell, will exceed the melting point of the steel. Such a case cannot be handled by the current code. In the survey of CFD calculations to be presented in section III, this difficulty occurred for only a single case, when the gun was driven extremely hard and incorporation of the steel droplets into the hydrogen was artificially suppressed. A solution was

obtained in this case by reducing the CFL number from 0.70 to 0.35, at the cost of doubling the CPU time. If the reduction of the CFL number does not produce a solution in a reasonable CPU time, the only alternative may be to increase the minimum steel cell thicknesses, at the cost of reducing the accuracy of the solution.

Barrel wall heat flux analysis in medium within bore– This analysis is described in some detail in Appendix A and, hence, will only briefly be outlined here. The analysis starts by deriving the basic equations for the skin friction and wall heat flux without mass addition (ablation of steel) at the barrel bore surface. Then, the wall heat flux is corrected (reduced) to account for the mass flux at the wall. The correction requires the calculation of a boundary layer reference temperature, for which an equation is derived. The mass addition analysis just referred to was derived in the references assuming that the medium injected at the wall is the same as the free-stream medium. For our calculations, this is not the case. Hence, a further correction is added, based on an experimental data base, to allow for the difference between the effective molecular weight of the medium injected at the wall and the free-stream medium. Finally, a last correction to the effective molecular weight of the free-stream medium is added, since the free stream is not, in general, pure hydrogen, but already contains some ablated steel. Further details can be found in Appendix A and the references.

Nonequilibrium turbulence model– A simple model (Appendix B) was developed which assumes that the nonequilibrium turbulence kinetic energy (TKE) relaxes towards the equilibrium value for the flow in question with an e-folding length which is multiple of the tube diameter. The basic model was presented previously, in Appendices A and B of reference 9, but has been slightly modified for the present version of the code. We take this opportunity to present the modified version of the nonequilibrium turbulence model, but present it in an appendix (Appendix B), since it is not the main topic of the present paper.

Coupling between barrel wall heat conduction model and wall heat flux calculation in the media within the bore– Three quantities must be exchanged between the two parts of the solution, the bore surface temperature and the bore surface heat and mass fluxes. The gridding in the axial direction is fixed for the heat conduction model within the barrel material but slides with the media zones for the in-bore media. The exchange of the three quantities just referred to is made using simple linear interpolations in the axial direction. However, when solutions first were obtained, they showed a violent oscillatory behavior with a period of two timesteps. The amplitude of the oscillations was, however, limited and the oscillations did not cause the solution to crash. The solutions for the wall heat conduction/wall heat and mass flux problem are only first order in time, although the CFD solution for the motion of the in-bore medium is second-order accurate in time and third-order accurate in space (ref. 9). What was needed to stabilize the wall erosion problem was, ideally, to change to a predictor-corrector method for the wall heat conduction/wall heat and mass flux problem. This would have required a fairly large amount of reprogramming, so that the following device was used instead. In calculating the reduction of the wall skin friction coefficient due to the wall mass flux, instead of simply using the single current value of the wall mass flux obtained from the parallel barrel heat conduction solution, an average of the current value and the value for the preceding timestep was used. In effect, the value from the preceding timestep is used as an estimate for the "corrector" value for the current timestep. This device was found to stabilize the solution for all cases run to date.

Update of cell variables in the in-bore– After the mass flux of steel from the barrel bore is calculated for a given cell in the in-bore medium for a given timestep, it is necessary to update the state variables of that cell. The steel is assumed to enter the in-bore medium as fine liquid droplets and to be instantly and completely mixed and equilibrated thermally and dynamically with the in-bore medium. The update is done by using the conservation of total mass, conservation of steel mass, conservation of momentum and conservation of energy equations. We start by calculating the increase in the steel mass of the cell, as follows.

$$\Delta m = m_w A \Delta t \tag{10}$$

where

Δm = increase of steel mass in cell

m_w = wall steel mass flux

A = cell wall area

Δt = timestep

The cell density change is given by

$$\rho' = \rho + \frac{\Delta m}{V} \tag{11}$$

where

ρ' = cell density after update

ρ = cell density before update

V = cell volume

The change in the hydrogen mass fraction of the cell is given by

$$m_1' = \frac{m_1}{1 + \frac{\Delta m}{\rho V}} \tag{12}$$

where

m_1' = hydrogen mass fraction after update

m_1 = hydrogen mass fraction before update

The change in the velocity of the medium in the cell is given by

$$u' = \frac{\rho u}{\rho'} \tag{13}$$

where

u' = velocity of medium in cell after update

u = velocity of medium in cell before update

The change in the internal energy in the cell is given by

$$e' = \frac{\rho}{\rho'}\left[e + \frac{u^2}{2}\left(1 - \frac{\rho}{\rho'}\right)\right] + \frac{\Delta m e_1}{\rho' V} \tag{14}$$

where

e' = internal energy in cell after update

e = internal energy in cell before update

e_1 = internal energy of molten steel just above the melting point

Equations (11)–(13) follow rather obviously from the corresponding conservation equations. Equation (14) is slightly more complicated, because e and e' are static internal energies and one must account for the change in kinetic energy during the update.

Grid convergence– The addition to the code of the capability to explicitly model gun erosion and the incorporation of the eroded barrel material into the working medium should have essentially no effect on the grid convergence of solutions. Grid convergence is very largely dependent upon the quality of the inviscid part of the solution for the in-bore media for the grids chosen. For this reason, no new grid convergence studies were made for the present version of the code. In reference 8, a grid refinement study was made for a version of the code without the ability to explicitly model erosion. Six griddings were studied, with the finest three grids being 14,14,52, 16,16,56 and 18,18,60. (The zones are gunpowder/gunpowder gas, polyethylene piston plastic and hydrogen working gas.) Taking the results for the finest grid as the standard, the differences in key pressures and velocities were 0.1–0.4% for the second finest grid and 0.6–1.0% for the third finest grid, except for the maximum contraction cone pressure, for which there were differences of 2.0% for the third finest grid. The gun survey of reference 8 was performed using the third finest gridding, for which the grid was judged to be adequately converged, to save CPU time. Further details of the grid refinement study can be found in reference 8. The original code was used to produce the gun optimization surveys of references 6 and 8. Almost all of the results for the present study were obtained with a gridding of 16,16,54, which is almost as fine as the second-finest gridding discussed above.

Miscellaneous final notes regarding solution techniques– The present algorithm does not model the deposition of steel from the hydrogen-steel mixture back onto the barrel bore surface. Thus, once ablated steel is incorporated into the hydrogen-steel mixture, it remains in the mixture indefinitely. Furthermore, there is no modelling of the incorporation of steel melted off the barrel wall into either the gunpowder/powder gas mixture or the plastic piston. For all solutions done to date, the barrel wall temperature in the gunpowder/powder gas zone remains far below the melting point, and thus the lack of the capability to incorporate melted steel from the barrel into the in-bore medium in this region produces no errors in the solution. Steel is lost from the bore surface in the region of the plastic piston in some of our solutions. However, the mass of the steel which might (perhaps) be incorporated into the plastic of the piston from this effect is so small compared to the piston mass (much less than 1%) that its effect on the solution would be negligible. On the other hand, it will be shown that the mass of steel which can be incorporated in to the hydrogen-steel cells can exceed 50% of the total mass in the cell, which obviously produces very large effects on the solution dynamics.

For most of the code modifications discussed above, no analytical solutions are available to check the accuracy of the code changes. Hence, for every code change made, the solution was checked to six-figure accuracy for one cell for one timestep using a hand calculator. A few errors were found this way and corrected. A representative solution has a gridding of 16,16,54 cells in the gunpowder/powder gas, piston plastic and hydrogen-steel zones, respectively, and runs at a CFL (Courant-Friedrichs-Lewy) number of 0.7. (Note that the outer two cells in each zone are “ghost” or boundary condition cells.) About 6000 steps are typically required until the projectile exits the muzzle. Such a solution requires about 8 minutes of single-processor CPU time on a Cray CM-90 machine. The code is rather inefficient and a full optimization effort could very likely make significant reductions in the time required to obtain a solution.

C. Gun and Conditions Modelled

Figure 1 shows a schematic sketch of one of the modelling configurations of the Ames 0.5" light gas gun. The numbers (in centimeters) are either the bore diameters or the distances from the blind end of the powder chamber. WG1–WG4 denote the whisker gauges used to measure piston velocity. In the calculations, the diaphragm is treated as a closed end boundary condition until the pressure at the diaphragm first exceeds the diaphragm rupture pressure; at that point the diaphragm is instantly removed. Table 1 shows the 45 shots which were modelled in this study. The variables listed in the table are

Shot number

Launch package mass

Powder mass

Piston mass (piston is polyethylene)

Powder type (the numbers are IMR/DuPont powder types)

Pump tube hydrogen fill pressure

Break valve (diaphragm) rupture pressure

Piston velocity (between whisker gauges 2 and 3)

Projectile muzzle velocity

Pump tube volume (nominal values)

Contraction cone angle (full angles)

The contraction cone is the conical section which joins the pump tube and the launch tube. There are four blocks of data in table 1, separated by horizontal lines. We will refer to these blocks of data as block 1, block 2, etc. The shots of block 1 were made at Ames Research Center in 1966; the shots of the remaining three blocks were made in 1995 and 1996. The gun configuration shown in figure 1 is exactly that for the CFD modelling of the first block of data. For the block 3 and block 4 data, all axial dimensions to the right of WG1 were reduced by 607.22 and 911.86 cm, respectively. In addition, for data in blocks 2, 3 and 4 with the 8.1 degree cone angle, the axial dimension at the large end of the cone was shifted to accommodate this cone angle. Where there are no entries in table 1 (e.g., piston and projectile velocities), those data were not obtained during the shots. About 80% of the shots shown in table 1 were modelled twice, once with the ablated (melted) steel incorporated into the hydrogen working gas and a second time where the ablation of the steel was fully modelled, but the steel was assumed to disappear after ablation. This allowed us to isolate the effect of loading the hydrogen gas with the ablated steel.

III. Results

The numerical results discussed in sections IIIA, IIIB and IIID below are, in all cases, from solutions in which the ablated steel from the bore has been incorporated into the in-bore working medium. Only in section IIIC below, where muzzle velocities will be discussed, will we discuss numerical results from solutions obtained both with and without incorporation of the ablated steel into the in-bore working medium.

A. Piston Velocities, Maximum Powder Pressures

Figures 2 and 3 show the comparisons of the experimental and theoretical piston velocities and maximum powder pressures for the shots of block 1 in table 1. The estimated uncertainties for the experimental piston velocities and maximum powder pressures are ±0.2% and ±2.5%, respectively. The piston velocities are those measured and calculated between whisker gauges 2 and 3 (see fig. 1). (We will denote whisker gauges 1, 2, etc., by WG1, WG2, etc., and we will also use the notations U_{12}, U_{23}, etc., for the piston velocities measured between WG1 and WG2, WG2 and WG3, etc.) We note that the powder burn rate and the piston coefficients of friction have been "tuned" to reproduce the observed maximum powder pressure and U_{23} for one selected shot. This is the shot 19/79 and the data points from this shot are marked with an asterisk in figures 2 and 3. This tuning is necessary because (1) in our two-stage guns the powder burns at a rate very different from that quoted by the manufacturer and (2) there is no good theory to predict, a priori, good values for the piston friction coefficients. The "tuning" process is discussed further in reference 9. Once the tuning has been done for the single shot selected, the parameters tuned are left untouched for all other calculations with the powder in question. Figures 2 and 3 show the very good agreement between the experimental and theoretical piston velocities and maximum powder pressures for the wide range of gun operating conditions in question. In addition to the experimental piston velocities U_{23}, the velocities U_{12} and U_{34} were also obtained for data block 1. During the tuning of the powder burn rate and the piston friction coefficients, no account was taken of these two additional experimental piston velocities and therefore the comparison of the experimental and theoretical values of U_{12} and U_{34} furnishes another check on the quality of the CFD solution. For U_{34}, the comparison is as good as or better than that shown in figure 2. For U_{12}, the comparison is

Table 1. Shots modelled on Ames 0.5" gun

Data block #	Shot #	Masses			Powder type	Pressures		Velocities		Pump tube volume	Contraction cone angle
		Launch (gms)	Powder (gms)	Piston (gms)		Hydrogen (bar)	Break valve (kbar)	Piston (m/sec)	Projectile (km/s)	(percent)	(degrees)
1	15/75	0.9473	175	917	4198	2.069	1.380	728.4	7.254	100	12.5
1	16/76	0.9296	175	917	4198	1.552	1.380	747.9	8.291	100	12.5
1	17/77	0.9115	175	888	4198	1.035	1.380	771.1	9.022	100	12.5
1	18/78	0.9239	175	905	4198	0.690	1.380	767.4	9.357	100	12.5
1	19/79	0.9122	200	900	4198	1.035	1.380	818.3	9.174	100	12.5
1	20/80	0.9407	200	888	4198	0.690	1.380	826.6	9.464	100	12.5
1	21/81	0.9475	225	888	4198	1.552	1.380	872.0	7.864	100	12.5
1	22/82	0.9873	225	888	4198	1.035	1.380	880.8	9.418	100	12.5
1	23/83	0.8897	200	1115	4198	1.552	1.380	744.3	8.108	100	12.5
1	24/84	0.9413	225	1115	4198	1.035	1.380	798.5	9.235	100	12.5
1	25/85	0.9649	250	1115	4198	1.035	1.380	844.3	9.147	100	12.5
1	27/87	3.0906	150	888	4198	2.069	0.690	670.5	4.968	100	12.5
1	28/88	3.0851	225	888	4198	2.069	0.690	861.0	6.325	100	12.5
1	29/89	0.8818	225	888	4198	1.035	0.690	877.8	9.150	100	12.5
1	30/90	3.1699	225	888	4198	1.035	0.690	877.8	6.721	100	12.5
1	31/91	0.9190	225	888	4198	1.035	0.690	880.8	8.839	100	12.5
1	33/93	0.7011	275	888	4198	0.690	1.380	981.4		100	12.5
2	623	1.406	190	821	4895	2.069	0.290	767.8	6.283	100	8.1
2	624	1.187	195	819	4895	1.655	0.290	793.7	7.041	100	8.1
2	625	1.172	195	821	4895	1.324	0.290	788.2	7.300	100	8.1
2	626	1.27	187	821	4895	2.069	0.290	760.1	6.245	100	8.1
3	627	1.169	195	709	4895	2.173	0.290	815.6	7.820	60	8.1
3	628	1.266	197	707	4895	1.697	0.290	822.9	8.062	60	8.1
3	632	1.1711	175	718	4895	3.394	0.290	710.5	5.621	60	8.1
3	633	1.2484	175	719	4895	2.704	0.290	740.3	6.495	60	8.1
3	637	1.2799	195	720	4895	2.049	0.290	787.0	7.529	60	8.1
3	638	1.2174	195	719	4895	2.049	0.290	755.6	7.163	60	8.1
3	641	1.205	185	719	4895	2.049	0.310	754.3	7.312	60	8.1
3	645	1.439	188	717	4895	2.049	0.310	766.2	6.892	60	8.1
3	647	1.1596	175	717	4895	3.394	0.310	731.5	5.774	60	8.1
4	651	1.2136	175	720	4895	4.056	0.310	680.9	6.706	40	8.1
4	653	1.3073	180	720	4895	4.035	0.310	698.6	6.910	40	8.1
4	661	1.414	178	718	4895	3.980	0.310	701.6	6.757	40	12.5
4	664	1.1636	170	718	4895	3.980	0.310	664.4	6.855	40	12.5
4	669	1.329	175	717	4895	3.083	0.310	642.2	7.148	40	12.5
4	672	1.166	172	716	4895	3.980	0.310	659.3	6.812	40	12.5
4	675	1.2135	175	718	4895	3.359	0.310	656.8	7.145	40	12.5
4	676	1.1663	173	718	4895	3.980	0.310	656.8	6.810	40	12.5
4	679	1.2589	195	717	4895	3.083	0.310	698.6	7.224	40	12.5
4	682	1.1836	173	717	4895	3.897	0.310	687.0	6.983	40	12.5
4	683	1.3996	180	717	4895	3.083	0.310	690.0	7.443	40	12.5
4	684	1.1909	175	712	4895	3.911	0.310	688.8	7.004	40	12.5
4	686	1.3462	195	715	4895	2.601	0.310	664.7	7.439	40	12.5
4	687	1.3563	215	711	4895	3.083	0.310	747.6	8.079	40	12.5
4	2144	1.069	219	710	4895	2.601	0.310			40	12.5

slightly worse than that shown in figure 2, with the scatter of the data points being about 50% greater than that shown in figure 2, and the experimental velocities being about 1.4% higher with respect to the theoretical values than those shown in figure 2. Nevertheless, the overall agreement between the experimental and theoretical piston velocities and maximum powder pressures for the shots of data block 1 was judged to be very satisfactory.

The comparison between the experimental and theoretical piston velocities for data block 2 is not shown here, but the agreement was as good as or better than that for the shots of data block 1. Figure 4 shows the comparisons of the experimental and theoretical piston velocities U_{23} for the shots of data blocks 3 and 4. The agreement between the theoretical and experimental values is reasonably good, but clearly inferior to that shown in figure 2 for data block 1. The scatter for figure 4 is between twice (for data block 3) and three times (for data block 4) that shown in figure 2. To understand the increased scatter in the piston velocity data for data blocks 3 and 4, we have investigated powder pressure data taken during shots 619–687. The most important grouping of powder pressure data for this study was taken between shots 651 and 684 in data block 4. This group includes 7 shots which are in data block 4 as well as 16 other shots with very similar gun operating conditions. The characteristics of the powder pressure pulses from these 23 shots (i.e., maximum pressure versus full duration of the pressure pulse at half maximum pressure) are plotted in figure 5. The estimated uncertainty for the durations of the pressure pulses is ±5%. It is very important to notice that, for all of the shots for which data are shown in figure 5, the critical gun operating parameters, powder mass, piston mass and pump tube hydrogen fill pressure vary by only 4.7%, 2% and 5%, respectively. Hence, these 23 shots were effectively made at nearly the same gun operating condition. The variation in maximum powder pressure should be only 5–10%, based on the variation of powder mass. Instead, the variation of the maximum powder pressure seen in figure 5 is about 58%. In addition, figure 5 shows a strong negative correlation between the maximum powder pressure and the duration of the pressure pulse defined by the full width at half maximum pressure. It is speculated that the latest series of piccolo tube igniters used to ignite the smokeless powder charges in the Ames 0.5" gun are extremely variable, much more so than those used previously. (Piccolo tube igniters are described in ref. 20.) This new series of igniters was used from shot 619 onwards. After the shots, the igniters were found to be in highly variable conditions. Some of the piccolo tubes were found virtually undamaged after use, others were found to be totally destroyed. Hence, it is believed that the ignition processes of the main smokeless powder charges in these shots were likely to have been highly variable. This is the most likely explanation for the large variations in the maximum powder pressures (for nearly identical shots) seen in figure 5. We are presently searching for a source of higher quality igniters.

We now perform statistical analyses of the variations of the piston velocities and maximum powder pressures (wherever data are available) for data blocks 1 to 4. We define r as the ratio of the experimental value to the corresponding CFD numerical value, as follows.

$$r = \frac{U_{23,ex}}{U_{23,nu}} \text{ or } \frac{P_{max,ex}}{P_{max,nu}} \tag{15}$$

where

P_{max} = maximum powder pressure

ex (subscript) denotes experimental value

nu (subscript) denotes numerical (CFD) value

r_{bar} is the average value of r and three statistical measures of the variability of r are defined as follows.

$$\Delta r_{max} = r_{max} - 1 \tag{16}$$

$$\Delta r_{min} = r_{min} - 1 \tag{17}$$

$$\Delta r_{rms} = \sqrt{\frac{\overline{r^2} - \bar{r}^2}{N}} \tag{18}$$

where

r_{max} = maximum value of r

r_{min} = minimum value of r

$\overline{r^2}$ = mean square value of r

$\bar{r}$ = mean value of r

N = number of points in data set

Table 2 shows the resulting statistical values. For the piston velocities, the data points for data block 1 are shown in figure 2 and those for data blocks 3 and 4 are shown in figure 4. (The data points for data block 2 are not shown.) For the maximum powder pressures, the data points for block 1 are those shown in figure 3 and those for selected shots of data block 4 (and other similar shots) are those shown in figure 5. Pressure data of sufficient quality for analysis were not available for data blocks 2 and 3. The various Δr values for the pressure variations are 2.2 to 3.1 times greater for data block 4 than for data block 1. This is in reasonably good agreement with the corresponding ratios of 3.1 to 3.5 for the corresponding piston velocity data. Thus, the increased scatter of the pressure data observed in figure 5 compared to that shown in figure 3 corresponds roughly to the increased scatter of

Table 2. Statistics for piston velocities and maximum powder pressures

Data blocks	Statistics of piston velocities					Statistics of maximum powder pressures				
	Δr_{rms}	Δr_{max}	Δr_{min}	r_{bar}	N	Δr_{rms}	Δr_{max}	Δr_{min}	r_{bar}	N
Block 1	0.0101	0.0277	–0.0112	1.0056	16	0.0457	0.0810	–0.1072	1.0211	14
Block 2	0.0064	0.0061	–0.0091	0.9997	4					
Block 3	0.0230	0.0344	–0.0387	1.0031	9					
Block 4*	0.0356	0.0463	–0.0730	1.0011	13	0.1010	0.3505	–0.2340	—	23

*For the powder pressure data, selected shots in data block 4 and shots with very similar gun operating parameters are included.

the piston velocity data shown in figure 4 compared to that shown in figure 2. Therefore, we believe that the increased scatter of the piston velocity data of figure 4 relative to that shown in figure 2 is a direct consequence of the increased variations in the way in which the powder is ignited and burns as a consequence of the variability of the current type of piccolo tube igniter used.

The shots used for the "tuning" of the powder burn rate and the piston friction coefficients for the 4895 powder were shots 672 and 676 in data block 4. The data from these shots are marked in figures 4 and 5. During the tuning operation, the correct piston velocity (see fig. 4) and maximum powder pressure (see fig. 5) were obtained, but the full width of the pressure pulse at half the maximum pressure was about 11% greater than that measured experimentally (see fig. 5). It was not possible to tune three parameters (piston velocity, maximum powder pressure and width of powder pressure pulse) by varying only two quantities—powder burn rate and piston friction coefficients.

We note that it very likely would be possible, in principle, to reduce the scatter in the piston velocities for data blocks 3 and 4 (see fig. 4) to the much lower amount of scatter seen in figure 2 for data block 1 by tuning the powder burn rates and the piston friction coefficients for each shot for which data are shown in figure 4. Tuning for every shot should be able to account for the variation in the powder burn rates due to the igniter variations referred to previously. Since it requires 6 to 10 CFD runs to tune to each different experimental condition, this could require of the order of 200 CFD tuning runs for the data shown in figure 4 and this was judged not to be feasible or worthwhile in the present research effort.

The agreement between the experimental and theoretical piston velocities and maximum powder pressures shown in figures 2 and 3 was judged to be very good and representative of what can be achieved with our CFD code and consistent ignition of the gunpowder. The agreement of the experimental and numerical piston velocities shown in figure 4 was judged to be reasonably satisfactory, though clearly inferior to that shown in figure 2, likely due to the increased variations in the piccolo tube igniters discussed above.

B. Gun Erosion

Erosion in the hydrogen/steel zone– Before discussing the comparison of the experimental and numerical gun erosion values, one must be aware of the difficulties inherent in making the experimental gun erosion measurements. These measurements involve inserting a telescoping gauge into the eroded gun barrel to the desired depth, positioning it parallel to the gun axis and at the maximum diameter, locking it, withdrawing it and then measuring the distance between the heads of the gauge with a micrometer. Typically, the diameter increase between shots is very small, of the order of 0.0025 cm, and is the difference between two measurements. Also, even if any actual given measurement were perfect, the eroded barrel shapes are highly irregular and a large number of different measurements could easily be obtained due to slight changes in the depth and the angle of the heads of the gauge. In short, the scatter of the barrel erosion measurements is often found to be rather large. The problem is obviously the worst for erosion measurements for a single shot. If a number of shots are made in succession at identical or nearly identical gun operating conditions, the total erosion can be measured with a much lower percentage error than for a single shot; the average erosion per shot is found by dividing by the total number of shots.

We note that no tuning whatsoever has been done on the method used to calculate the gun erosion. The only tuning performed in the present analysis is that described in section IIIA regarding the gunpowder burn rate and the piston coefficients of friction.

For the block 1 data (table 1), the original measurements of the barrel diameter have been lost, but the launch package diameters are available and are observed to increase steadily as the barrel erodes. From these projectile diameters, we were able to calculate the gun

erosion for 12 of the block 1 shots shown in table 1. The projectile is placed in the barrel at approximately 4 calibers depth beyond the break valve; hence, we will compare the experimental erosion values with those predicted by the CFD calculations at this location. The comparison of these experimental and numerical gun erosion values is shown in figure 6. (The estimated uncertainties for the experimental erosion values are ±0.002 calibers/shot, as shown in the figure.) The trend line of the experimental measurements is within 10–20% of the predicted value. Eight of the twelve individual experimental values are within ±40% of the predicted values and all but one of the experimental values are within a factor of 2 of the predicted values. Given that these are erosion values for single shots subject to the considerable uncertainties shown for the reasons described above, we consider this agreement very satisfactory.

For the leftmost data point, note that the numerical erosion value is actually within the uncertainty band of the experimental value, which is ±0.002 calibers/shot. It is also important to realize that, for the erosion model developed herein, if the barrel wall temperature does not exceed the melting point, the barrel erosion will be exactly zero. In reference 21 and the references quoted therein, it is pointed out that solid barrel material can be removed due to erosion mechanisms other than melting. Hence, the experimental erosion value for this data point could really be as high as 0.002 calibers and be due to mechanisms not modelled in the present CFD code. It does appear, however, that the postulated melting mechanism for the bore erosion gives, overall, reasonably good predictions of the experimental erosion values shown in figure 6.

In data block 3, four shots (shots 635–638) were taken with nearly identical gun operating conditions. For each of these four shots, barrel diameters were measured at four different depths into the barrel. From these data, we obtained the average erosion values (per shot) at the four different depths into the barrel. Greater accuracy would be expected for these experimental gun erosion values than for those values based on single shots (such as those shown in figure 6). Figure 7 shows the resulting comparison between experimental and numerical gun erosion values. (The error bars show the estimated uncertainties of ±0.0004 calibers/shot in the experimental erosion measurements.) The abscissa in the figure is the depth into the barrel, in calibers, from the diaphragm station (see fig. 1). The numerical gun erosion values are those calculated for shot 637, which are essentially identical to those calculated for shot 638. The agreement is excellent. All of the experimental values are within 20% of the numerical values. The numerical erosion values fall within the uncertainty bands of the experimental data.

None of the erosion data shown in figures 6 or 7 was taken deeper than about 16 calibers into the barrel. A new barrel was installed in the gun just before shot 650 and was used for all shots until shot 687, plus two additional shots, shots 2143 and 2144. Thus, this barrel, at the end of its life, had been subject to the total erosion for these 40 shots. The shots on this barrel included the 15 shots of data block 4 in table 1, plus 25 other shots at gun operating conditions very similar to selected shots in data block 4. This barrel was then removed and cut up into eight sections, allowing measurements to be made throughout the barrel. These measurements are shown as the solid line in figure 8. Note that near the barrel cuts at ~120, ~155 and ~215 calibers the barrel diameter curve shows what appears to be irregularities in shape. It is believed that these are not, in fact, real irregularities in the shape of the barrel, but rather reflect the errors inherent in measuring the barrel diameter. From these apparent variations in barrel diameter, the errors in the barrel diameter measurements are estimated to be ±0.0006 calibers. From the CFD simulations made for the 15 shots of data block 4, it was determined that only 8 shots would produce any erosion. These are shots 669, 675, 679, 683, 685, 686, 687 and 2144. For all other shots, the barrel wall temperature at all points between the diaphragm and the muzzle always remains below the melting point, and hence, no erosion is predicted. The erosion values for these eight shots were added together and used to calculate the numerically determined barrel diameter curve shown in figure 8.

To obtain the experimental barrel diameter curve in figure 8, it was necessary to make an estimate of the amount of material removed during the barrel honing operations. In a series of 40 shots made on a single barrel, the barrel must be honed a number of times to keep it sufficiently smooth that good launches can be obtained. Thus, during the series, barrel material is lost due to true erosion during the shots and, also, due to honing. We have no way of directly determining the amount of material removed during honing. An estimate can be made, however, as follows. It is seen from figure 8 that the experimental barrel diameter between 130 and 220 calibers into the barrel is essentially constant, within the accuracy of the barrel measurements. Also, in this depth range, the numerically predicted barrel erosion is seen to be essentially zero. However, material has been removed in this region due to honing. To generate the experimental barrel diameter curve shown in figure 8, the amount of material removed by honing in the range of 130–220 calibers into the barrel has been assumed to apply throughout the barrel. This technique cannot, of

course, provide any information on possible variations of the amount of material removed by honing with axial position.

The apparent barrel erosion near the muzzle was judged to most likely be an artifact of the honing, as follows. Several of the most erosive CFD solutions were allowed to run considerably beyond the time at which the projectile exits the muzzle. In no cases was the barrel wall temperature in the region near the muzzle predicted to rise anywhere near the melting point. Hence, the numerical erosion predictions in the region near the muzzle would always be zero. We believe that the apparent erosion near the muzzle is most likely due to an increased amount of material removed there during honing. Near the muzzle and the diaphragm ends of the barrel, the hone can tilt more severely than in the central regions of the barrel. Further, it is likely that the hone spends more time near the two ends of the barrel than in the central regions of the barrel. This effect could also be responsible for the relatively high apparent experimental barrel erosion seen in figure 8 for the first 15 calibers (and, in particular, for the first 4 calibers) of depth into the barrel.

For depths into the barrel between 5 and 50 calibers, we see that the experimental values are within a factor of 2 of the numerical predictions. For depths from 50 to 100 calibers into the barrel, the CFD results overpredict the erosion by factors increasing from ~2 at 50 calibers depth to 3–4 at 100 calibers depth. This difference is not explainable by any reasonable variation in the amount of material removed by honing, and very likely represents a true deficiency in the current modelling techniques. For example, if material melted off the barrel wall, say, at 0–15 calibers into the barrel is redeposited on the wall in the region 50–100 calibers into the barrel, this would reduce the actual erosion in the latter region to below that which could be predicted by the current theory. This is, of course, the effect seen in this region in figure 8. (The current theory, as noted earlier, cannot model redeposition of steel from the hydrogen-steel mixture back onto the barrel bore.)

Overall, we believe the agreement shown in figures 6–8 between the experimental and numerical erosion values is reasonably good, considering the complexity of the processes modelled and the fact that the erosion calculations were not tuned in any way. Further support for the erosion modelling will be provided in the comparisons of the experimental and numerical muzzle velocities to be made in section IIIC.

Erosion in the plastic (piston) zone– Returning to figure 8, we note that there is a zone of erosion in the contraction cone, between distances of –20 and 0 calibers "depth into the barrel." This is not due to erosion by the hydrogen-steel mixture but, rather, by the piston friction against the wall of the contraction cone and, possibly, by the direct retreat of the steel wall due to the very high pressures in the contraction cone (see sec. IIIC). In this section, we will make a comparison of experimental and numerical values for erosion of one of the contraction cone sections by the piston. (We will make no attempt to calculate the direct retreat of the contraction cone wall due to the high pressures.) We consider the contraction cone section listed in table 1 with the 8.1 degree angle. For this contraction cone section, we made a plastic cast of the conical section bore, removed it and measured its diameters at a number of different axial locations. By comparing these diameters with those given on the original machinist's drawing of the contraction cone section, we determined the total wall retreat for the section at a number of different axial locations.

The contraction cones are used for much longer time periods than the barrels. In fact, for the entire life of the Ames 0.5" gun, back to 1964, it appears that only two contraction cones have been used, one with a nominal angle of 12.5 degrees and the other with an angle of 8.1 degrees. About 460 shots on the 0.5" gun are logged in the Ames log books. For some of the shots, the contraction cone used is identified; for others, it is not. We considered all shots where we know that the contraction cone in question was used and (for want of better information) one-half of the shots for which the contraction cone section is not identified. All of the shots except for 33 were done with the full (100%) pump tube volume. The 33 shots made with 60% and 40% pump tube volumes are those shown in table 1 in data blocks 3 and 4 and other shots made under very similar conditions. In reference 22, experimental erosion data at 4 calibers depth into the barrel is given for the Ames 0.5" gun for gun configurations with 100%, 60% and 40% pump tube volume. The erosion for 60% pump tube volume is roughly half that for 100% pump tube volume. The erosion for 40% pump tube volume is 4–10 times less than that for 100% pump tube volume. Based on these numbers, we have ignored the erosion in the contraction cone for the shots with 40% pump tube volume and considered the erosion for the shots made with 60% pump tube volume to be equivalent to the erosion of half that number of shots at full pump tube volume.

Most of the shots on the 8.1 degree contraction cone section were made with the full pump tube volume, piston masses of about 900 g and hydrogen fill pressures of 2.07 bar. A wide range of powder masses, from 60 to 275 g, was used. A number of CFD runs for these conditions with various powder masses were made. A diaphragm rupture pressure of 690 bar and a projectile mass of 1.27 g, which are representative for a large

number of the tests in question, were used in these calculations. It was found that the piston produced no contraction cone erosion for powder masses of 140 g or less. Hence, to estimate the numerically determined contraction cone erosion, we limited ourselves to the estimated 118 shots made with powder masses greater than 140 g. The average powder mass for these shots was 195 g. Hence, we calculate the contraction cone erosion for a shot with the full pump tube volume, a piston mass of 900 g, a projectile mass of 1.27 g, a diaphragm rupture pressure of 690 bar, a hydrogen fill pressure of 2.07 bar and a powder mass of 195 g. The contraction cone wall retreat calculated this way (for a single shot) is then compared with the experimental value deduced from the diameter measurements of the eroded contraction cone section. The total wall retreat measured experimentally is divided by our estimated number of erosive shots (118) to provide an experimental value of the average wall retreat per shot.

The comparison of the experimental and numerically determined wall retreat for the 8.1 degree contraction cone is shown in figure 9. The format of figure 9 differs from that of figures 6–8 in that calibers are not used since we are dealing with a conical section. Rather, the absolute wall retreat in centimeters is used for the ordinate. Stating the uncertainties in the experimental erosion values of figure 9 requires some care. If the assumed number of shots on the contraction cone section was exactly correct, the only uncertainty in the experimental erosion values would be due to the measurement error, which is estimated to be ±0.00002 cm, or about the size of the symbols. On the other hand, if the assumed number of shots on the contraction cone section was in error by, say, 30%, the experimental erosion values of figure 9 would also be in error by this percentage. It seems probable that the uncertainties in the experimental erosion values in figure 9 due to the uncertainty in the number of shots on the contraction cone are less than 30%, but this is not certain.

In figure 9, the abscissa is the distance from the blind end of the powder chamber (see fig. 1). The locations of the start of the contraction cone and the diaphragm are marked in the figure. Two aspects of figure 9 show rather good agreement between the experimental and numerical results: these are the maximum amount of wall retreat and the axial location of the start of wall retreat. Wall retreat is predicted and observed experimentally to start near the beginning of the contraction cone. This might be expected, since at this point the bearing pressure on the piston surface will increase rather abruptly, due to jamming into the conical section.

The obvious difference between the experimental and numerical results shown in figure 9 is that the numerically predicted erosion drops to zero at ~1617 cm and remains zero until 1634 cm, whereas the experimentally observed erosion actually peaks between 1617 and 1635 cm. This disagreement is almost certainly due to the deep hollow cone machined into the front of the plastic piston (see, e.g., ref. 9), which cannot be modelled by our quasi-one-dimensional CFD code. For the numerically predicted erosion curve shown in figure 9, the front of the (one-dimensional) cone comes to a halt at ~1617 cm and, thus, cannot produce erosion farther down the contraction cone section. Because the hydrogen gas velocities are much lower in the contraction cone than in the barrel, the convective heat transfer from the hydrogen gas is correspondingly lower, and the hydrogen gas does not begin to produce erosion in the contraction cone until very close to the diaphragm location at 1636 cm. Thus, the numerically predicted erosion remains zero between 1617 and 1634 cm. On the other hand, the experimental reality is that the hollow cone in the piston collapses as the piston enters the contraction cone section, which allows the most forward parts of the piston plastic to project much farther into the contraction cone than the 1617 cm numerically predicted limit seen in figure 8. For some of the higher energy shots, the piston plastic ends up nearly filling the contraction cone section and even, in extreme cases, extends well into the launch tube.

The basic mechanism and magnitude of the erosion of the contraction cone by the piston appears to be reasonably well predicted by the present model. Yet, there are appreciable differences in the axial distribution of the contraction section erosion due to the inability of the present quasi-one-dimensional formulation to model the strongly two-dimensional flow at the forward end of the deforming piston.

C. Muzzle Velocity

General– Figures 10–13 show plots of experimental versus numerically predicted muzzle velocity values for the four data blocks of table 1. The uncertainties in the experimental muzzle velocities are estimated to be ±0.3%. Most of the experimental muzzle velocities have been plotted versus two different numerically predicted (CFD) muzzle velocities. For the circle data points, the theoretical muzzle velocity was calculated with the complete CFD solution, allowing for the loading of the hydrogen gas with the steel ablated from the barrel wall. For the cross data points, the CFD solution has the full frictional and heat transfer losses from the hydrogen to the barrel wall, including the heat losses necessary to ablate the steel from the wall. However, the steel, after

being ablated (melted) off the wall, was assumed to disappear. Thus, the difference between the circle and the cross data points represents the effect of the loading down of the hydrogen by the steel ablated from the barrel wall. For a total of seven low velocity data points in data blocks 3 and 4, no calculations were made without hydrogen loading, because it was judged that, for these points, there would be no barrel erosion. For two very high velocity shots (one in each of data blocks 1 and 4), there are no actual experimental muzzle velocity data, due to either projectile breakup or instrumentation failure. For these cases the “experimental muzzle velocity” shown in the figure was estimated by scaling from the next lower velocity data point or group of data points. In each of the four plots, the heavy solid line is the line of perfect agreement between experiment and theory. Note that the ranges of the coordinates for figures 10–13 vary from figure to figure.

The comparisons made in figures 10–13 cover a very wide range of gun operating parameters, as listed below.

Powder masses: 150–275 g

Powder types: IMR/DuPont 4198, 4895

Piston masses: 710–1115 g

Projectile masses: 0.88–3.17 g

Hydrogen load pressures: 0.69–4.06 bar

Diaphragm rupture pressures: 0.29–1.38 kbar

Pump tube volumes: 100%, 60% and 40% of initial benchmark value

Experimental projectile muzzle velocities: 4.97–9.46 km/sec

Over this wide range of gun operating parameters, the agreement between the experimental muzzle velocities and the numerically predicted velocities calculated including loading of the hydrogen by the ablated steel was very good. Overall, about two-thirds of the muzzle velocities agreed within 0.5 km/sec and the worst disagreements were about 0.7 km/sec. For the data of blocks 2–4, projectiles (typically spheres) were launched with four-piece sabots. The four-piece sabots are more subject to drive gas blow-by and a consequent loss of muzzle velocity. (Reference 23 gives evidence of muzzle velocity shortfalls for the Ames 0.28" gun of 0.3 km/sec up to 0.8–1.0 km/sec—the latter for poorly made projectiles.) The shots of data block 1 were made with solid polycarbonate slugs, which are less subject to blow-by. For this data block, the agreement of the muzzle velocities is even better, with two-thirds of the muzzle velocities agreeing within 0.35 km/sec, the remaining one-third of the data points having disagreements up to 0.5 km/sec and a single data point having an error of 0.7 km/sec.

Previous modelling of the Ames 0.5" gun (ref. 8) had been performed using an earlier version of the present code which did not allow for loading of the hydrogen gas with the ablated barrel material. Using that version of the code, a muzzle velocity was obtained without loading of the hydrogen. Then, from the measured increase in barrel diameter, an estimate was made of the amount of erosion for the shot in question. Finally, a heuristic correction was applied to reduce the calculated muzzle velocity to allow for loading of the hydrogen. This past procedure, although better than applying no correction at all for hydrogen loading, had a number of substantial limitations. First, it was based on a very restricted data base—five shots on the Ames 0.5" gun. Second, it required an actual measurement of the erosion for the shot in question to be made, thus it did not permit true a priori predictions to be made. Third, the muzzle velocity errors were considerably larger than those of the present technique. For the four high velocity shots of figure 11 of reference 8, the errors were 0.8, 0.6, 0.95 and 0.8 km/sec. The current procedure, in which a direct calculation is made of the barrel erosion and the loading of the hydrogen gas with ablated barrel material, is much superior in all respects. It should be applicable to any size gun, makes a priori predictions and has yielded considerably more accurate predictions of muzzle velocity. It has yielded excellent muzzle velocity predictions even for the very severe gun operating conditions producing the experimental muzzle velocities of 8.0–9.5 km/sec shown in table 1 and figures 10–13.

If we look at the differences between the experimental muzzle velocities and the numerically predicted muzzle velocities calculated without loading of the hydrogen (cross data points in figs. 10–13), there are large disagreements at the higher velocities. In data blocks 2–4, there are disagreements of 1 km/sec at experimental muzzle velocities of 6.9–7.2 km/sec, increasing up to nearly 2 km/sec at the highest experimental muzzle velocities for each data block. For data block 1, the maximum disagreements are even larger, reaching 3–4 km/sec at experimental muzzle velocities of 9.0–9.5 km/sec. Clearly, the higher muzzle velocities cannot be properly predicted without taking into account the loading of the hydrogen by the ablated barrel wall material.

Except for the three data points for the heavy (~3 g) projectiles in data block 1, it is clear that for each of figures 10–13, there is reasonably well-defined muzzle velocity at which the loading of the hydrogen with ablated barrel material starts rather abruptly. Below this muzzle velocity, little or no barrel ablation/erosion is predicted. We will now proceed to study this effect further and, also,

to investigate the effect of pump volume on the ablation of barrel wall material. We first consider each shot from table 1, where, from figures 10–13, there are two numerically predicted muzzle velocities, one without hydrogen loading and one with hydrogen loading; we then form the ratio of these two velocities. (We will denote this ratio of velocities by R_v.) This provides a measure of the amount of hydrogen loading with ablated barrel wall material for each shot in point. If R_v is unity, there is no loading of the hydrogen. (Note that R_v is not linear in the amount of hydrogen loading.) We will then plot R_v versus the experimental normalized muzzle velocity. The normalized muzzle velocity is used to attempt to remove the effect of variation of projectile mass for the shots of table 1 and figures 10–13. We define the normalized muzzle velocity, $u_{m,n}$, as follows.

$$u_{m,n} = u_{m,t}\left(m_{proj} / 1.27\right)^{.5} \qquad (19)$$

where

$u_{m,t}$ = true muzzle velocity

m_{proj} = projectile mass

$u_{m,n}$ is normalized, on an energy basis, to a projectile mass of 1.27 g, which is a representative mean value for most of the shots of table 1 and figures 10–13. The normalization of the muzzle velocity is only a rough method to account for the variation of projectile mass. The method works reasonably well for projectile masses in table 1 between 0.70 and 1.44 g. It did not work well for the three shots in data block 1 with the very heavy (~3 g) projectiles. Hence, we will omit these three shots in the comparisons we are about to make.

Figure 14 shows a plot of R_v versus the normalized experimental muzzle velocity. The data for data blocks 1 and 2, with 100% pump tube volume, were found to collapse very well together and are considered as a single data grouping in the figure (cross data points). The data for data blocks 3 and 4 with, respectively, 60% and 40% pump tube volume, are shown in the figure by the circle and square data points. Trend lines, which are simple linear fits, are shown for each of the three data groupings. For each data grouping, there is a considerable amount of variation around the trend line. This is very likely because each muzzle velocity (for a given pump tube volume) can be achieved using many different combinations of powder mass, hydrogen fill pressure and diaphragm rupture pressure. Different combinations of gun operating parameters will produce different amounts of hydrogen loading. Nevertheless, figure 14 shows a well-defined trend for a reduction in hydrogen loading (and, hence, wall ablation/erosion) as the pump tube volume is reduced from 100% to 60% to 40%. For each pump tube volume, the one or two data points in figure 14 at the lowest normalized muzzle velocities show essentially no hydrogen loading ($R_v < 1.01$). From these data points, we can estimate the normalized muzzle velocity at the onset of hydrogen loading for the three different pump tube volumes. These velocities are 6.25, 6.45 and 6.70 km/sec for pump tube volumes of 100%, 60% and 40%, respectively, showing the advantage of reduced pump tube volume.

As a more specific example of the strong reduction of hydrogen loading with decreased pump tube volume, we consider normalized muzzle velocities between 7.5 and 8.0 km/sec. From figure 14, we see that, in this muzzle velocity range, R_v decreases from 1.31–1.42 at 100% pump tube volume to 1.18–1.25 at 60% pump tube volume to 1.15–1.22 at 40% pump tube volume. Reference 24 shows experimentally observed reductions in gun erosion with decreasing pump tube volume for the Ames 0.5" gun for the same normalized muzzle velocity range. The great reduction in gun erosion seen in reference 24 as the pump tube volume is decreased from 100% to 60% to 40% corresponds well with the trends in R_v versus pump tube volume shown in figure 14.

To obtain normalized muzzle velocities of 7.5–8.0 km/sec, the gun must be driven much harder in the 100% pump tube volume configuration than in the 40% pump tube volume configuration, due to the much more severe weighing down of the hydrogen working gas with ablated wall material. To study this further, for each one of the shots represented in figure 14, we have taken the calculated maximum pressures in the contraction cone and at the projectile base and plotted them against the experimental normalized muzzle velocity. These results are shown in figures 15 and 16. For the maximum pressures in the contraction cone (fig. 15), the results for data blocks 1 and 2 again collapsed together very well and are shown as one data grouping in the figure. For the maximum pressure at the projectile base (fig. 16), the results for data blocks 1 and 2 did not collapse together and, hence, all four data blocks are shown separately in the figure. Again, for all data groupings in figures 15 and 16, simple linear trend lines have been fit. In figure 15, due to the data scatter, little difference can be seen between the results for 60% and 40% pump tube volume. However, it is clear that the maximum pressures in the contraction cone for the 100% pump tube volume range from 1.5 to 1.6 times those for the smaller pump volumes for the lower muzzle velocities up to 1.8 to 1.9 times those for the smaller pump volumes for the higher muzzle velocities. For the 7.5–8.0 km/sec normalized muzzle velocity range, for the 100% pump tube volume configuration, maximum contraction cone pressures of 24,000–31,000 bar are required, whereas for the lower

pump tube volume configurations, these pressures are reduced to 13,000–16,500 bar. This gives another indication that the gun must be driven considerably harder in the 100% pump tube volume configuration than in the 40% or 60% pump tube volume configurations to achieve the same muzzle velocities. For the maximum pressures at the projectile base (fig. 16), the differences between the results for the different pump tube volumes are considerably smaller, the maximum pressures generally being about 500 bar higher for the 100% pump tube volume configuration than for the configurations with lower pump tube volumes. This means that the projectile will undergo maximum base pressures 10–20% higher with the larger pump tube volume. Part of the reduction in the maximum base pressures on switching from data block 1 (100% pump tube volume) to data blocks 3 and 4 may, however, be due to the reduction in the diaphragm rupture pressure from 0.69–1.38 to 0.29–0.31 kbar (see table 1). This is illustrated by the fact that the maximum projectile base pressures are about 500 bar lower for data block 2 at 100% pump tube volume and 0.29 kbar diaphragm rupture pressure than for data block 1 at 100% pump tube volume and 0.69–1.38 kbar diaphragm rupture pressure.

Summing up, it is clear that the gun must be driven much harder in the 100% pump tube volume configuration than in the 40% pump tube volume configuration to achieve high muzzle velocities. This is clear from the much higher hydrogen loading, gun erosion and maximum contraction cone pressures which occur for the larger pump tube volume configuration. In addition, there are also somewhat (10–20%) higher maximum projectile base pressures for the 100% pump tube volume configuration.

It is possible that further reductions in hydrogen loading, gun erosion, and maximum pressures in the contraction cone and at the projectile base (for one and the same normalized muzzle velocity) could be obtained by further reductions of pump tube volume. To date, this has not been tested at Ames, either numerically or experimentally. The reduction in pump tube volume cannot be continued indefinitely to produce improved gun performance, since, eventually, there will be insufficient compression to heat the hydrogen sufficiently to achieve the sound speeds needed for high velocity launches. From the work presented here, the optimum pump tube volume for the Ames 0.5" gun is no greater than 40% of the original value and could even be less than this value.

Maximum muzzle velocities– In 1970, reference 25 published a plot of muzzle velocities versus normalized launch mass [= (launch mass)/(barrel diameter)^3] for a large number of launchers in a number of different research establishments. In this same plot, a limiting curve of muzzle velocity versus normalized launch mass is shown. We will focus on the high velocity portion of this curve, between launch velocities of 7 and 11.5 km/sec. Although this limiting curve was published nearly 30 years ago, it has proven very difficult to surpass using a reusable launcher launching controlled-shape projectiles. Based on the discussion in the previous subsection, it seems that a major factor creating this limiting line (where it is shown in ref. 25) is the loading down of the hydrogen working gas with the ablated barrel wall material. The fastest experimental muzzle velocity shown in figure 10 is still about 1 km/sec below the limiting line of reference 25. The extremely high velocity shot shown in figure 10 (where the projectile did not survive the launch and the experimental muzzle velocity is therefore only an estimate) approaches the limiting line.

To study this further, we have taken muzzle velocity and maximum pressure data from figures 10–13, 15 and 16. For each data block, we have considered two shots. First, we have considered the highest muzzle velocity shot for which hydrogen loading was predicted to be very minor. The second shot for each data block was the maximum velocity shot for which actual muzzle velocity data were obtained. For these maximum velocity shots, loading of the hydrogen was always predicted to be very substantial. For each one of these pairs of shots, we have noted in table 3 the two experimental muzzle velocities (u_{exp}) and the difference between them (Δu_{exp}), and the numerically predicted muzzle velocities without loading of the hydrogen ($u_{nu,nh}$) and the difference between them ($\Delta u_{nu,nh}$). Also shown in the table are the calculated maximum pressures in the contraction cone ($p_{max,cc}$) and at the projectile base ($p_{max,pb}$) for the shots with loading of the hydrogen gas with ablated barrel wall material. We will concentrate on data block 1 because it contains the highest muzzle velocities. The striking point about the velocities shown in table 3 for data block 1 is the very large (5.44 km/sec) increase in muzzle velocity predicted as one changes from the low H_2 loading condition to the high H_2 loading condition if the loading of the hydrogen is ignored. For the high H_2 loading condition, a muzzle velocity of ~13 km/sec is predicted. Note also the very large increases in maximum contraction cone and projectile base pressures predicted as one moves from the low H_2 loading condition to the high H_2 loading condition. The former increases from 6,600 to 30,000 bar and the latter from 2,000 to 5,000 bar. (These numbers are calculated for the shots with loading of the hydrogen.) Thus, the high H_2 loading condition is much more violent than the low H_2 loading condition. In spite of this, the muzzle velocity increase actually achieved (2.21 km/sec) is very much smaller than that predicted when the loading of the hydrogen is ignored (5.44 km/sec). Similar results

Table 3. Data for very high muzzle velocity shots

Data block #		1	2	3	4
$u_{nu,nh}$ (km/sec)	Low H_2 loading	7.49	6.71	7.31	7.64
$u_{nu,nh}$ (km/sec)	High H_2 loading	12.94	9.29	9.84	10.01
$\Delta u_{nu,nh}$ (km/sec)		5.44	2.58	2.53	2.37
u_{exp} (km/sec)	Low H_2 loading	7.25	6.25	6.50	7.00
u_{exp} (km/sec)	High H_2 loading	9.46	7.30	8.06	8.08
Δu_{exp} (km/sec)		2.21	1.05	1.56	1.08
$p_{max,cc}$ (bar)	Low H_2 loading	6,580	6,530	6,490	7,420
$p_{max,cc}$ (bar)	High H_2 loading	30,340	13,010	17,430	17,610
$p_{max,pb}$ (bar)	Low H_2 loading	2,050	1,160	1,450	1,570
$p_{max,pb}$ (bar)	High H_2 loading	5,050	2,260	3,390	3,700

at somewhat lower maximum muzzle velocities were noted in data blocks 2–4. In these cases, the muzzle velocity increases actually achieved (1.05–1.56 km/sec) were also much smaller than those predicted when the loading of the hydrogen is ignored (2.37–2.58 km/sec). Thus, loading of the hydrogen with the ablated wall material appears to be very effective in limiting the maximum attainable muzzle velocities and likely explains, at least in part, why it is very difficult to surpass the limit curve of reference 25 using reusable launchers launching controlled-shape projectiles.

D. CFD Snapshots

To understand, in a little more depth, the loading of the hydrogen with the ablated barrel wall material, we have taken CFD snapshots within the barrel of the progress of the solution of one of the more erosive shots. We have chosen shot 687, the most erosive shot of data block 4 for which actual muzzle velocity was obtained. Profiles of hydrogen mass fraction, density and pressure are plotted at nine different times. These are shown in figures 17–19. The location of the (ruptured) diaphragm is indicated in the figures and the muzzle is located off the figures to the right at 1107.58 cm. For each time shown, the projectile base is located at the right end of the curve. This location is somewhat obscure for the earlier times in figure 17 due to overlapping of the curves, but is more apparent in figures 18 and 19.

In figure 17, we see that a large amount of the loading of the hydrogen with ablated wall material takes place between the first and the last time step shown. We note that the maximum hydrogen loading for this shot is very large. For the heaviest hydrogen loading for the last timestep shown, the working fluid is 75% steel and only 25% hydrogen. Even heavier maximum hydrogen loadings would be expected for the most erosive shots in data block 1. In figure 18, we can see the large “humps” in density due to the loading of the hydrogen with steel, particularly for the last five timesteps shown. If we consider the last timestep shown, the total mass of the working medium between the diaphragm and the projectile can be estimated to be ~9 gm. If we draw a line excluding the steel “hump” from this curve, we can estimate that about 40% of the mass of the working medium, or ~3.6 gm, is ablated steel from the barrel. This mass of ablated steel is very significant when compared to the projectile mass of 1.36 gm. A great deal of the energy in the hydrogen gas must go into accelerating the ablated steel; this same portion of the hydrogen energy is therefore unavailable to accelerate the projectile. Figure 19, particularly for the last five timesteps, shows the severe drop in the driving pressure as one traverses the working medium region with the heavy loading with ablated steel. The pressure gradients in these regions are used to accelerate (largely) the ablated steel and result in a large drop in the pressure available at the projectile base. During the last five timesteps, the projectile base pressure drops from 2000 to 270 bar as the projectile moves from 818 to 1009 cm. As the projectile moves from 818 to 892 cm, it accelerates from 6.02 to 7.18 km/sec; after traversing another 117 cm, it has gained only another 0.3 km/sec, due to the precipitous drop in base pressure. It is recognized that, in this portion of the launch cycle of a gun, there is a rather rapid drop in projectile base pressure even in the absence of ablation of barrel material and the consequent loading up of the hydrogen with same. However, this pressure drop is very much increased when the

hydrogen is loaded up with ablated barrel wall material. In the CFD modelling of shot 687, the calculated muzzle velocity was 10.01 km/sec with no hydrogen loading; this was reduced to 8.20 km/sec when hydrogen loading was taken into account. Thus, a loss of muzzle velocity of ~1.8 km/sec was predicted due to hydrogen loading. The experimental muzzle velocity was 8.08 km/sec, in good agreement with the CFD value when hydrogen loading is taken into account.

IV. Summary and Conclusions

A well-validated quasi-one-dimensional CFD code for the analysis of the internal ballistics of two-stage light gas guns was modified to explicitly calculate the ablation of steel from the gun bore and the incorporation of the ablated wall material into the hydrogen working gas. The modifications were the construction of an equation-of-state for the hydrogen-steel mixture, the heat conduction analysis in the steel, the calculation of the heat flux from the in-bore media to the wall and the coupling of the solutions in the steel and the in-bore media.

The modified code was used to model 45 shots made with the NASA Ames 0.5" light gas gun under an extremely wide variety of gun configurations and operating conditions. The 45 shots were divided into four data blocks: for the first two data blocks, the pump tube volume was the original standard value, and for data blocks 3 and 4, the pump tube volume was reduced to ~60% and ~40% of the original value, respectively. Agreement between the experimental and numerically predicted piston velocities was excellent for data blocks 1 and 2. The experimental values ranged from about 1% below to about 3% above the predictions. For the same shots, the agreement of the maximum powder pressures was very good. The experimental values ranged from 11% below to 8% above the predictions. The agreement for the piston velocities for data blocks 3 and 4 was reasonably good, but showed more variation than the piston velocities for data blocks 1 and 2. The experimental values ranged from about 7% below to about 5% above the predictions. This greater piston velocity variation for data blocks 3 and 4 was most likely due to wide variations in the performance of the igniters for the powder charge of the gun for these data blocks. The maximum powder pressure variations for data block 4 were found to be very large, up to ±30%, due, most likely, to the variations in igniter performance.

For a wide variety of gun operating conditions in data block 1, experimental and numerical gun erosion values at 4 calibers depth in the barrel were compared. The trend line of the experimental measurements was within 10–20% of the numerically predicted line, eight of the twelve individual experimental values were within ±40% of the predicted values and all but one of the experimental values are within a factor of 2 of the predicted values.

For conditions of data block 3, experimental measurements of gun erosion were made at depths of 4, 8, 12 and 16 calibers into the barrel for four shots under nearly identical operating conditions. These experimental measurements were compared with CFD calculations and excellent agreement was obtained, with all of the experimental values being within 20% of the CFD values. For the conditions of data block 4, experimental measurements of gun erosion were made throughout the gun barrel after a series of 40 shots. For depths into the barrel between 5 and 50 calibers, the experimental values were within a factor of 2 of the numerical predictions. For depths from 50 to 100 calibers into the barrel, the CFD results overpredict the erosion by factors increasing from ~2 at 50 calibers depth to 3–4 at 100 calibers depth. Overall, the agreement between the experimental and numerical gun erosion values was judged to be reasonably good, considering the complexity of the processes modelled and that the CFD erosion calculations were not “tuned” in any way to improve agreement with the experimental results.

Gun erosion due to frictional heating of the steel wall by the plastic piston was also modelled and good agreement was obtained between the experimental and numerical values for the maximum amount of material eroded.

Experimental muzzle velocities were compared with numerically predicted muzzle velocities calculated with and without loading of the hydrogen gas with the ablated barrel wall material. These comparisons were made over the following very wide range of gun operating parameters.

Powder masses: 150–275 g

Powder types: IMR/DuPont 4198, 4895

Piston masses: 710–1115 g

Projectile masses: 0.88–3.17 g

Hydrogen load pressures: 0.69–4.06 bar

Diaphragm rupture pressures: 0.29–1.38 kbar

Pump tube volumes: 100%, 60% and 40% of initial benchmark value

Projectile muzzle velocities: 4.97–9.46 km/sec

The agreement between the experimental muzzle velocities and the numerically predicted velocities calculated including loading of the hydrogen by the ablated steel was very good. Overall, about two-thirds of the

muzzle velocities agreed within 0.5 km/sec and the worst disagreements were about 0.7 km/sec. The current procedure, in which a direct calculation is made of the barrel erosion and the loading of the hydrogen gas with ablated barrel material, is much superior to the earlier procedure (ref. 8) used at Ames where a calculation was first made without hydrogen loading and then a heuristic correction factor, based on experimental gun erosion data, was applied to allow for hydrogen loading. At the higher velocities, there are large disagreements between the experimental muzzle velocities and the numerically predicted muzzle velocities calculated without loading of the hydrogen. These disagreements range from 1 to 2 km/sec in data blocks 2–4 up to 3 to 4 km/sec in data block 1. Clearly, the higher muzzle velocities cannot be properly predicted without taking into account the loading of the hydrogen by the ablated barrel wall material.

Comparison of results for the 100%, 60% and 40% pump tube volumes shows that, at the higher muzzle velocities, operation at 40% pump tube volume provides superior performance, with much lower hydrogen loading, ~4 times less gun erosion (ref. 24), ~40% lower maximum pressures in the gun contraction cone and 10–20% lower maximum pressures at the projectile base.

Large muzzle velocity gains were predicted upon driving the gun harder when hydrogen loading is not taken into account; much smaller muzzle velocity gains were predicted when hydrogen loading is taken into account and were achieved in practice. Thus, loading of the hydrogen with the ablated wall material appears to be very effective in limiting the maximum attainable muzzle velocities and likely explains, at least in part, why it is very difficult, when launching a controlled-shape projectile, to surpass a muzzle velocity limit curve published nearly 30 years ago (ref. 25). CFD snapshots of the hydrogen mass fraction, density and pressure of the in-bore medium were presented for a very erosive shot. These snapshots showed a very heavy maximum loading of the hydrogen with the ablated barrel material. This leads to large pressure drops in the region of heavy hydrogen loading and consequent large drops in projectile base pressure.

Appendix A

Gun Bore Wall Heat Flux Analysis

The calculation of the skin friction and the heat flux at the barrel bore starts with the following equations, slightly modified from those of Appendix A of reference 9, for the case without erosion of barrel material.

$$\tau_{wo} = \frac{1}{2} C_{fo} \rho_\infty |u_\infty| u_\infty \tag{A1}$$

$$q_{wo} = \frac{1}{2} C_{fo} \rho_\infty |u_\infty| \left[\left(e_\infty + \frac{p}{\rho_\infty} \right) \left(1 - \frac{T_w}{T_\infty} \right) + \frac{u_\infty^2}{2} \right] \tag{A2}$$

where

τ_{wo} = skin friction at the bore surface

C_{fo} = skin friction coefficient at the bore surface

ρ_∞ = density of medium within the bore

u_∞ = velocity of medium within the bore

q_{wo} = heat flux at bore surface

e_∞ = internal energy of medium within the bore

p = pressure of medium within bore

T_w = bore surface temperature

T_∞ = temperature of medium within the bore

The derivation of equations (A1) and (A2) is standard and is given in Appendix A of reference 9; hence, we will not repeat it here. For the case of the heat transfer from the plastic piston material to the barrel bore, we use the following equation, taken from Appendix C of reference 9.

$$q_{wo} = \frac{1}{2} \tau_{wo} u_\infty \tag{A3}$$

For the case of erosion of the barrel surface due to heating by the hydrogen gas, we will have a reduction of C_{fo} to C_f due to the wall blowing effect of the molten steel being lost. We calculate this reduction using the equation of figure 8 of reference 26, which can easily be transformed to yield the following equation.

$$\frac{C_f}{C_{fo}} = \frac{1}{\left[1 + 3.83 \frac{m_w}{\rho_\infty |u_\infty|} \left(\frac{\rho_\infty}{\rho^*} \right)^{.5} \left(\frac{2}{C_{fo}} \right)^{.5} \left(\frac{C_{fo}}{C_f} \right)^{.25} \right]^3} \tag{A4}$$

where

C_{fo} = skin friction coefficient without mass addition

C_f = skin friction coefficient with mass addition

m_w = wall mass flux

ρ^* = density of free-stream medium at the reference temperature, T^*

We evaluate the reference temperature by starting with equation (25) of reference 26, as follows.

$$T^* = 0.5(T_w + T_\infty) + 0.2(T_{ro} - T_\infty) + 0.1 \frac{m_w}{\rho^* u_\infty} \frac{1}{C_{ho}^*} (T_w - T_\infty) \tag{A5}$$

where

T^* = reference temperature

T_w = wall temperature

T_∞ = free-stream static temperature

T_{ro} = free-stream recovery temperature

and C_{ho}^* is given by

$$C_{ho}^* = \frac{q_{wo}}{\rho^* u_\infty C_p (T_{ro} - T_w)} \tag{A6}$$

where

q_{wo} = wall heat flux without mass addition

C_p = specific heat of free-stream medium

Since ρ^* appears only to the 0.5 power in equation (A4) and the last term of equation (A5) is generally a fairly small correction, we will use a number of approximations in evaluating the latter term; these make the analysis much more tractable. The approximations include assuming $h = C_p T$ in several places, where h is the enthalpy, assuming proportionality between h and T in several places and assuming $h_{ro} = h_\infty + 0.5(u_\infty)^2$. ($h_{ro}$ is the free-stream recovery enthalpy.) With these assumptions, equations (A5) and (A6) can be modified to yield

$$h^* = 0.5 h_\infty \left(\frac{T_w}{T_\infty} + 1 \right) + 0.1 u_\infty^2 + z h_\infty \left(\frac{T_w}{T_\infty} - 1 \right) \tag{A7}$$

and

$$z = \frac{0.1 m_w}{q_{wo}} \left[h_\infty \left(1 - \frac{T_w}{T_\infty} \right) + \frac{u_\infty^2}{2} \right] \tag{A8}$$

where

h_∞ = enthalpy of free-stream medium at free-stream temperature

h^* = enthalpy of free-stream medium at reference temperature

We limit z as follows.

$$0 \le z \le 0.5 \qquad \text{(A9)}$$

The lower limit is imposed because z should never be negative, since it expresses a proportionality between the heat flux and the driving (total) temperature difference. The upper limit is imposed because if z exceeds 0.5, then, for low velocity flows, T* could be outside the range between T_∞ and T_w, which is impossible. After calculating h* from h_∞ using equations (A7) and (A8), we make the further approximation

$$\frac{\rho^*}{\rho_\infty} = \frac{h_\infty}{h^*} \qquad \text{(A10)}$$

and take the value of ρ^*/ρ_∞ from equation (A10) and insert it in equation (A4) to allow one to calculate C_f (with wall mass flux).

Equation (A4), from reference 26, was derived for mass addition of the same medium which is in the free-stream flow. We make a correction for injection of "foreign medium" (usually "foreign gas") as follows. The term m_w in equations (A4) and (A8) is multiplied by the factor

$$\left(\frac{\overline{m}_e}{\overline{m}_w} \right)^{.67}$$

where

$\overline{m}_e$ = effective molecular weight of free-stream gas (or medium)

$\overline{m}_w$ = molecular weight of gas or medium injected at the wall

to correct for the molecular weight difference between the free-stream medium and the medium injected at the wall. This correction procedure was derived in reference 27, using the analyses and data given in references 28 and 29. We take the basic values for the molecular weights of hydrogen and steel to be 2.0 and 55.85, respectively. (We use this procedure even though it is recognized that the steel enters the in-bore medium as liquid droplets, not as a gas.) If there is already steel incorporated into the hydrogen working gas in the gun tube bore, we take the effective molecular weight of the medium within the bore to be $2/m_1$, where m_1 is the mass fraction of hydrogen in the medium within the bore. Thus, in general, we take

$$\overline{m}_e = 2 / m_1 \qquad \text{(A11)}$$

Appendix B

Nonequilibrium Turbulence Model

A simple model was developed which assumes that the nonequilibrium turbulence kinetic energy (TKE) relaxes towards the equilibrium value (TKE_{eq}) for the flow in question with an e-folding length (L_e) which is a multiple of the tube diameter. (The e-folding length is the length over which the difference between the nonequilibrium and equilibrium TKE will relax to 1/e times its original value in a steady, constant area flow.) Hinze (ref. 30) presents an extensive discussion of the fully developed low speed turbulent pipe flow measurements of Laufer (ref. 31). We estimate L_e using (1) Laufer's graphs (presented in Hinze) of the TKE production distribution across the pipe radius, (2) Laufer's graphs (also presented in Hinze) of the TKE production distribution across the pipe radius and (3) Schlichting's (ref. 32) values for the ratio of maximum to mean velocity for low speed, fully developed pipe flow. From these data for $Re_D = 5 \times 10^5$, we estimate $L_e = 3.27 \times$ (pipe diameter). (Re_D is the Reynolds number of the pipe flow based on the pipe diameter.) The range of Re for hydrogen flow in the pump tube and barrel of our two-stage light gas guns is typically 3×10^5 to 3×10^7. The Reynolds number for the data of references 30 and 31 is within our range, but towards the low end of it. However, turbulent pipe flow does not appear to change very rapidly with Re over the Re range of interest (at least over the range 3×10^5 to 3×10^6 reported in reference 33). Hence, we use the value of L_e given above as a rough estimate in our CFD model. The relaxation term in our model thus becomes

$$d(TKE) = \frac{\Delta x}{L_e}\left(TKE - TKE_{eq}\right) \qquad (B1)$$

where d(TKE) is the change in TKE which takes place when the flow moves a distance Δx, and we use

$$TKE_{eq} = 0.00929u^2 \qquad (B2)$$

where u is the mean flow velocity in the tube, which is also taken from the data of Laufer (ref. 31) for $Re_D = 5 \times 10^5$. For simplicity in the equations, we have dropped the subscript "neq" from TKE_{neq}; i.e., "TKE" in the present equations denotes TKE_{neq}. For one timestep Δt, the distance that the flow moves is simply $u\Delta t$. Since the tube changes diameter, in the gun model, L_e is not fixed, but is taken to equal to $R_L D$, where $R_L = 3.27$ as discussed above and D is the local tube diameter. Inserting these two results into equation (B1) yields the following equation for the relaxation term of the TKE equation.

$$d(TKE) = \frac{u\Delta t}{DR_L}\left(TKE_{eq} - TKE\right) \qquad (B3)$$

A difficulty with equation (B3) is that, as it stands, there will be no TKE relaxation if the velocity, u, goes to zero. Since the TKE will obviously relax due to the turbulent motion itself, even if u = 0, we have modified equation (B3) by replacing u with

$$\beta = \max\left(u, \sqrt{\frac{1}{2}\left(u^2 + \frac{TKE}{0.00929}\right)}\right) \qquad (B4)$$

Thus, our final form of the relaxation term of the TKE equation is

$$d(TKE) = \frac{\beta\Delta t}{DR_L}\left(TKE_{eq} - TKE\right) \qquad (B5)$$

To calculate the changes of TKE within any cell over a timestep, equation (B5) is used, along with the usual terms taking account of the convection of TKE across the cell boundaries of cells.

With the nonequilibrium TKE values known, the skin friction coefficient, C_f, at the bore surface of the gun is corrected as follows. The correction is applied only in the transition and turbulent flow regimes, with $Re_D > 1828$. First, we calculate

$$\zeta = \max\left[\left(\frac{TKE}{TKE_{eq}}\right), 1\right] \qquad (B6)$$

Then, the skin friction coefficient is corrected using ζ as follows.

$$C_{f,turb,corr} = C_{f,lam} + \left(C_{f,turb,un} + C_{f,lam}\right)\zeta^{.5} \qquad (B7)$$

where

$C_{f,turb,corr}$	=	corrected turbulent skin friction coefficient
$C_{f,lam}$	=	laminar skin friction coefficient
$C_{f,turb,un}$	=	uncorrected turbulent skin friction coefficient

ζ is required to be greater than or equal to unity so that $C_{f,turb,corr}$ must be greater than or equal to $C_{f,turb,un}$ and never less than the latter value.

References

1. Canning, T. N.; Seiff, A.; and James, C. S.: Ballistic Range Technology. AGARDOgraph 138, August 1970, pp. 11–95.
2. Ebihara, W. T.; and Rorabaugh, D. T.: Mechanisms of Gun-Tube Erosion and Wear. In Gun Propulsion Technology, L. Stiefel, ed., vol. 109, Progress in Aeronautics and Astronautics, AIAA, Washington, 1988, pp. 357–376.
3. Canning, T. N.; Seiff, A.; and James, C. S.: op. cit., pp. 41–44.
4. Chavez, D. J.; King, C. C.; and Linley, L. L.: A Study to Optimize a 7.6-mm (30-caliber) Two-Stage Light Gas Gun. Presented at the 42nd Aeroballistic Range Association Meeting, Adelaide, South Australia, October 21–25, 1991.
5. DeWitt, J. R.: Configuration Development of the New AEDC 3.3 Inch Launcher. Presented at the 45th Aeroballistic Range Association Meeting, University of Alabama at Huntsville, Huntsville, Alabama, October 10–14, 1994.
6. Bogdanoff, D. W.; and Miller, R. J.: Optimization Study of the Ames 1.5" Two-Stage Light Gas Gun. AIAA Paper 96-0099, presented at the 34th AIAA Aerospace Sciences Meeting, Reno, Nevada, January 15–18, 1996.
7. Bogdanoff, D. W.; and Miller, R. J.: Recent Developments in Gun Operating Techniques at the NASA Ames Ballistic Ranges. NASA TM-110387, March 1996.
8. Bogdanoff, D. W.: Optimization Study of the Ames 0.5" Two-Stage Light Gas Gun. NASA TM-110386, March 1996.
9. Bogdanoff, D. W.; and Miller, R. J.: New Higher-Order Godunov Code for Modelling Performance of Two-Stage Light Gas Guns. NASA TM-110363, September 1995.
10. Ahmad, I.: Problem of Gun Barrel Erosion; An Overview. In Gun Propulsion Technology, L. Stiefel, ed., vol. 109, Progress in Astronautics and Aeronautics series, AIAA, New York, 1988, p. 315.
11. Lampman, S. R.; Zorc, T. B.; Ronke, A. W.; Henry, S. D.; and Daquila, J. L., eds.: Metals Handbook, 10th ed., vol. 1, published by the American Society for Metals, 1990, p. 152.
12. Boyer, H. E.; and Gall, T. L., eds.: Metals Handbook, Desk Edition, published by the American Society for Metals, 1985, pp. I-63 to I-64.
13. Touloukian, Y. S.; Powell, R. W.; Ho, C. Y.; and Klemens, P. G.: Thermal Conductivity, Metallic Elements and Alloys. Plenum, New York, 1970, pp. 1214–1215.
14. Holman, J. P.: Heat Transfer. 6th ed., McGraw-Hill, New York, p. 635.
15. Touloukian, Y. S.; and Buyco, E. H.: Specific Heat; Metallic Elements and Alloys. Plenum, New York, 1970, pp. 639–640, 730–731.
16. Weast, R. C.; and Astle, M. J.: CRC Handbook of Chemistry and Physics. 61st ed., CRC Press, Boca Raton, Florida, 1980, p. D-62.
17. Touloukian, Y. S.; Kirby, R. K.; Taylor, R. E.; and Desai, P. D.: Thermal Expansion, Metallic Elements and Alloys. Vol. 12 in the series Thermophysical Properties of Matter, Plenum, New York, 1975, p. 157.
18. Washburn, E. W., editor-in-chief: International Critical Tables of Numerical Data, Physics, Chemistry and Technology. McGraw-Hill, New York, 1926, Vol. I, p. 102; Vol. II, p. 463.
19. Holman, J. P.: op. cit., p. 161.
20. Varney, A. M.: Primers and Igniters. In Gun Propulsion Technology, L. Stiefel, ed., vol. 109, Progress in Astronautics and Aeronautics series, AIAA, New York, 1988, pp. 22–24.
21. Bogdanoff, D. W.: Reduction of Gun Erosion and Correlation of Gun Erosion Measurements. Presented at the 48th Meeting of the Aeroballistics Range Association, Institute of Advanced Technology, University of Texas at Austin, Austin, Texas, November 3–7, 1997, p. 1.
22. ibid., pp. 2–4, figure 2.
23. Bogdanoff, D. W.; and Miller, R. J.: New Higher-Order Godunov Code for Modelling Performance of Two-Stage Light Gas Guns. NASA TM-110363, 1995, pp. 28–29.
24. Bogdanoff, D. W.: Reduction of Gun Erosion and Correlation of Gun Erosion Measurements. Presented at the 48th Meeting of the Aeroballistics Range Association, Institute of Advanced Technology, University of Texas at Austin, Austin, Texas, November 3–7, 1997, figure 2.

25. Canning, T. N.; Seiff, A.; and James, C. S.: op. cit., p. 87.

26. Knuth, E. L.; and Dershin, H.: Use of Reference States in Predicting Transport Rates in High-Speed Turbulent Flows with Mass Transfer. International Journal of Heat and Mass Transfer, vol. 6, 1963, pp. 999–1018.

27. Bogdanoff, D. W.: Ram Accelerator Direct Space Launch System: New Concepts. Journal of Propulsion and Power, vol. 8, March–April 1992, pp. 488–489 (Appendix C).

28. Tauber, M. E.: A Review of High-Speed Convective Heating Computational Methods. NASA TP-2914, July 1989, p. 19.

29. Jeromin, L. O. F.: The Status of Research in Turbulent Boundary Layers with Fluid Injection. Progress in Aeronautical Sciences, vol. 10, 1970, pp. 153–162.

30. Hinze, J. O.: Turbulence. 2nd ed., McGraw-Hill, New York, 1975, pp. 724–742.

31. Laufer, J.: The Structure of Fully Developed Pipe Flow. NACA TN-1174, 1954.

32. Schlichting, H.: Boundary Layer Theory. 7th ed., McGraw-Hill, New York, 1979, pp. 599–600.

33. ibid., pp. 598–612.

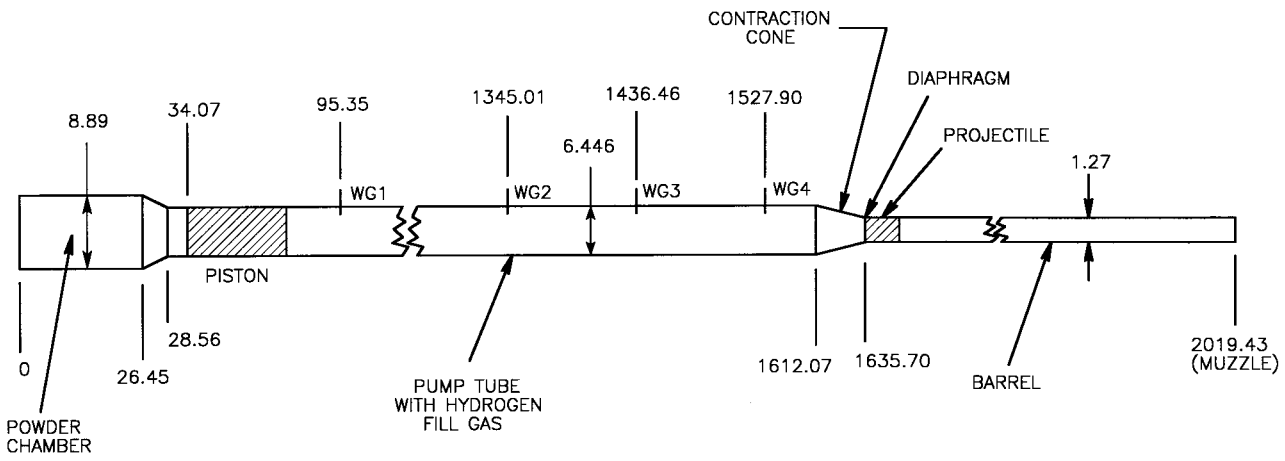

Figure 1. Schematic sketch of Ames 0.5" two-stage light gas gun. Numbers (in centimeters) are bore diameters or distances from the blind end of the powder chamber. WG1–4 denote whisker gauges for measurement of piston velocity.

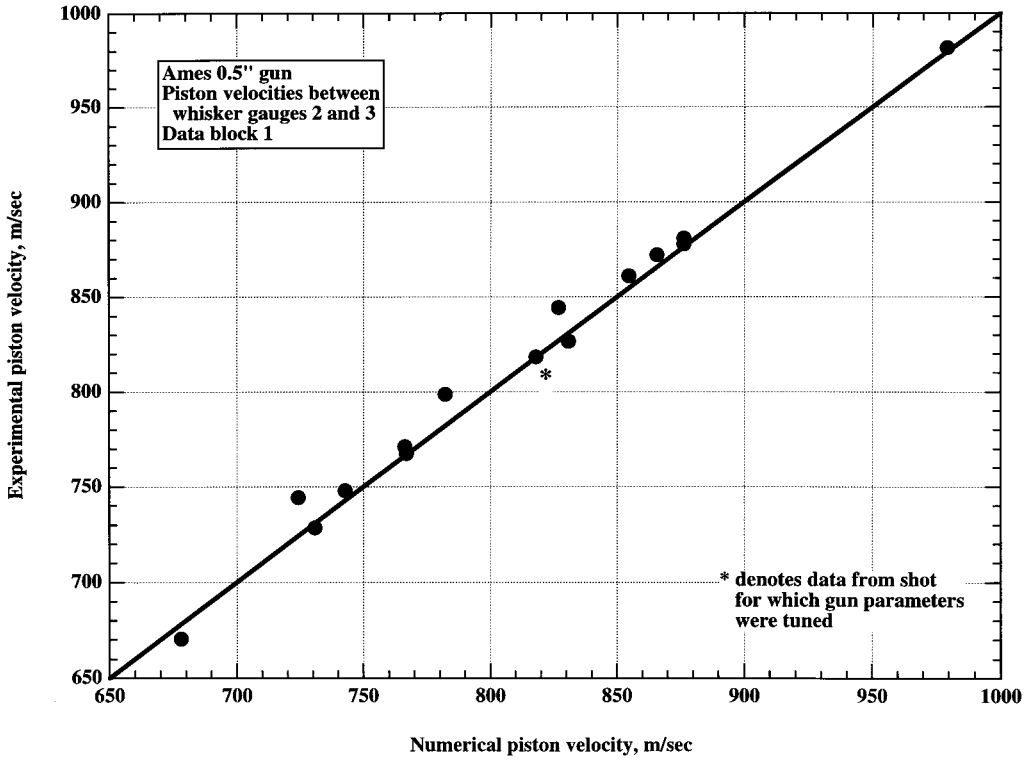

Figure 2. Experimental and numerical piston velocities for Ames 0.5" gun for data block 1.

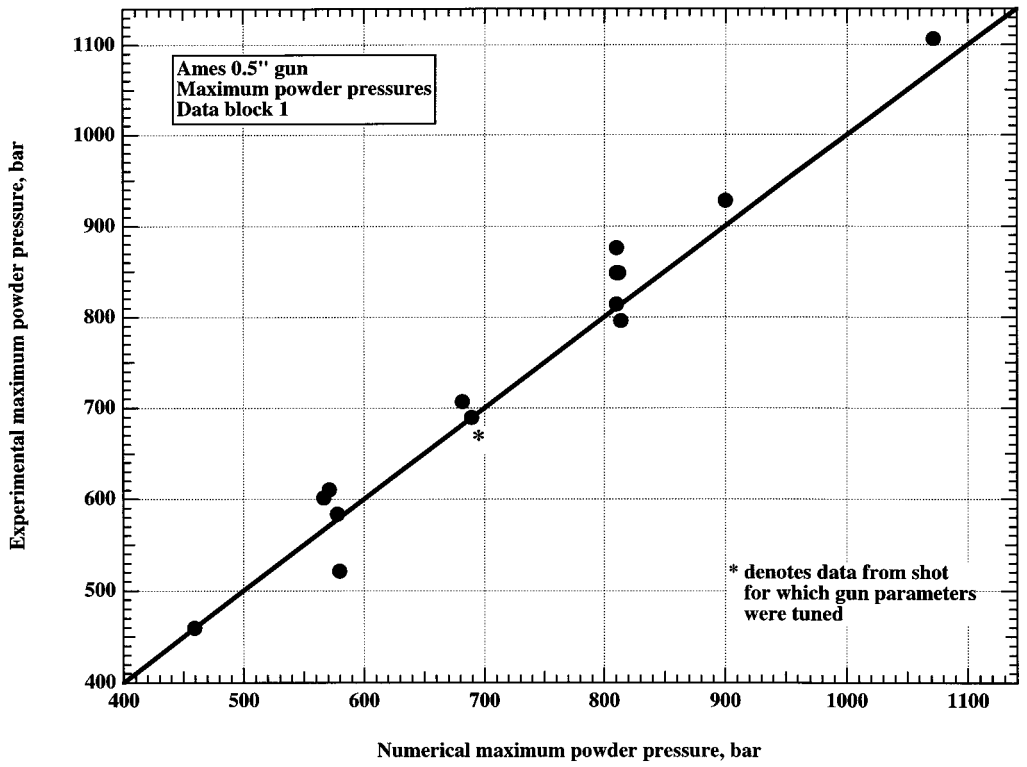

Figure 3. Experimental and numerical maximum powder pressures for Ames 0.5" gun for data block 1.

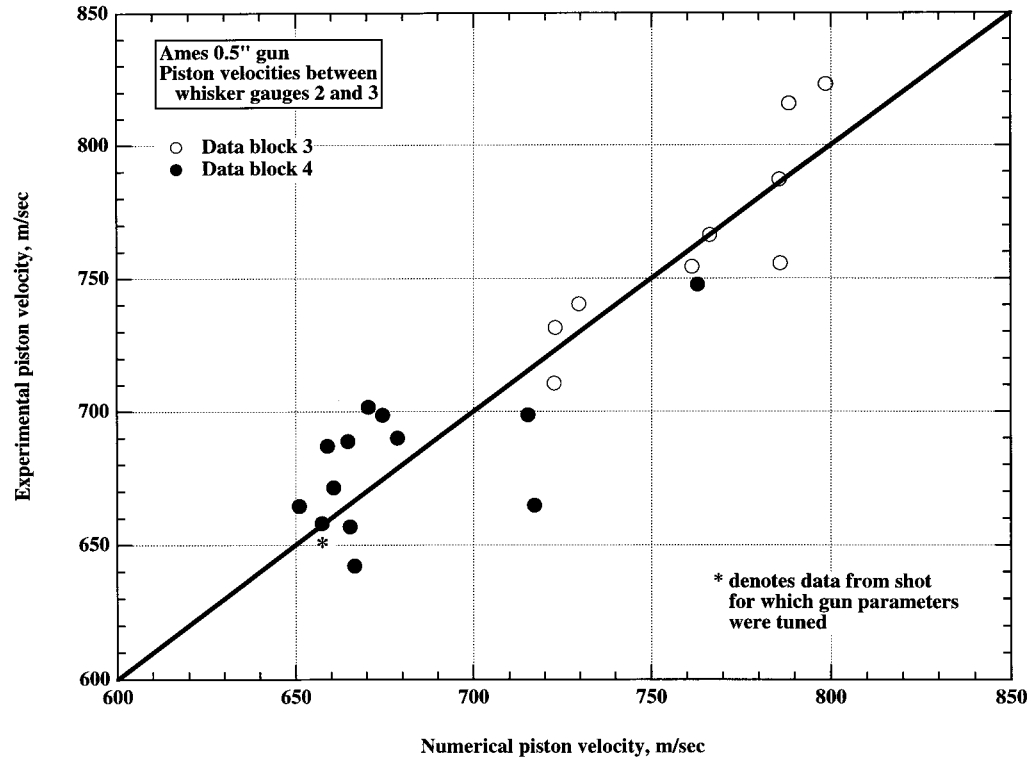

Figure 4. Experimental and numerical piston velocities for Ames 0.5" gun for data blocks 3 and 4.

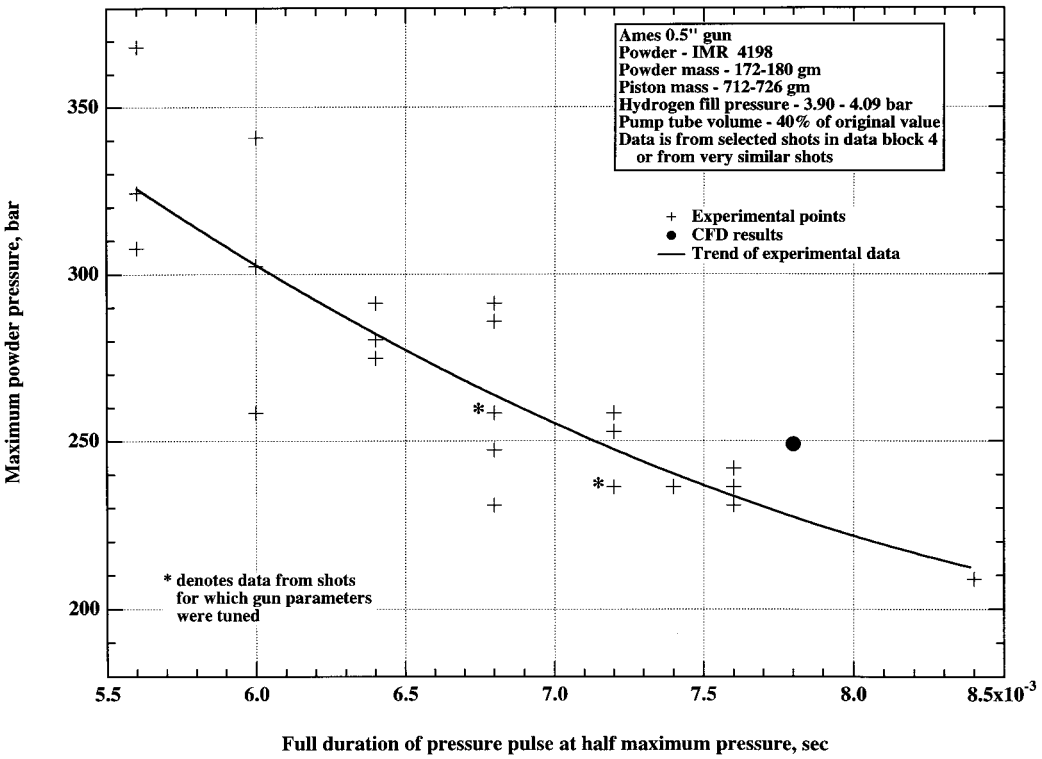

Figure 5. Characteristics of powder pressure pulses for selected shots in data block 4 and for very similar shots.

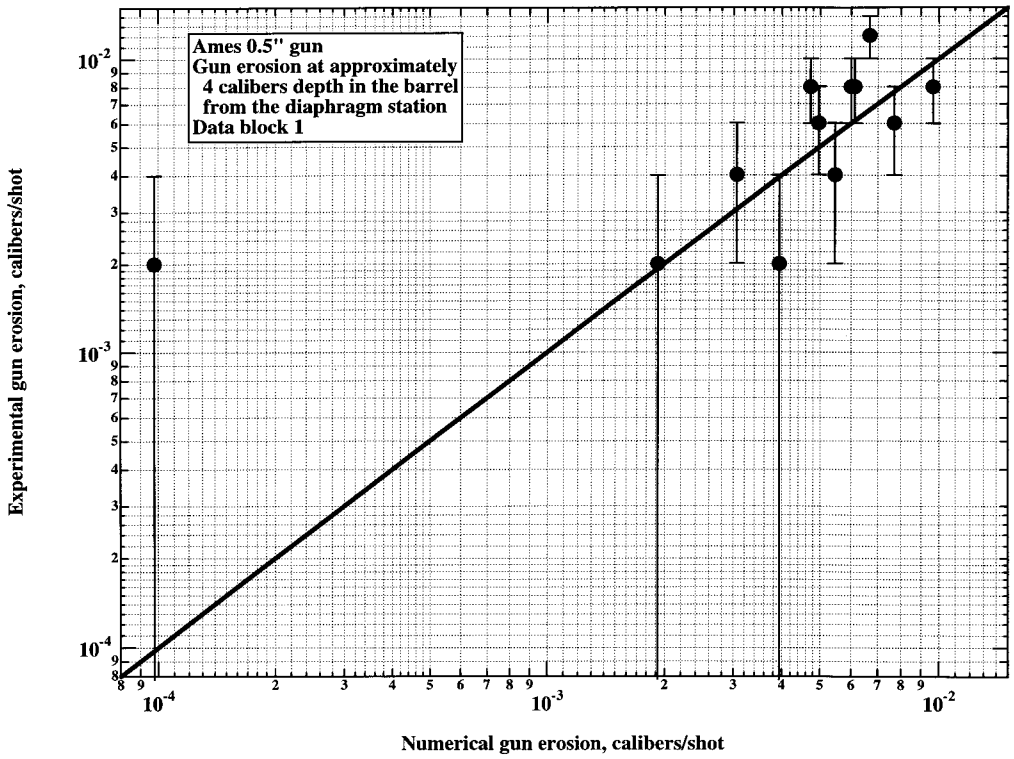

Figure 6. Experimental and numerical gun erosion values for Ames 0.5" gun for data block 1.

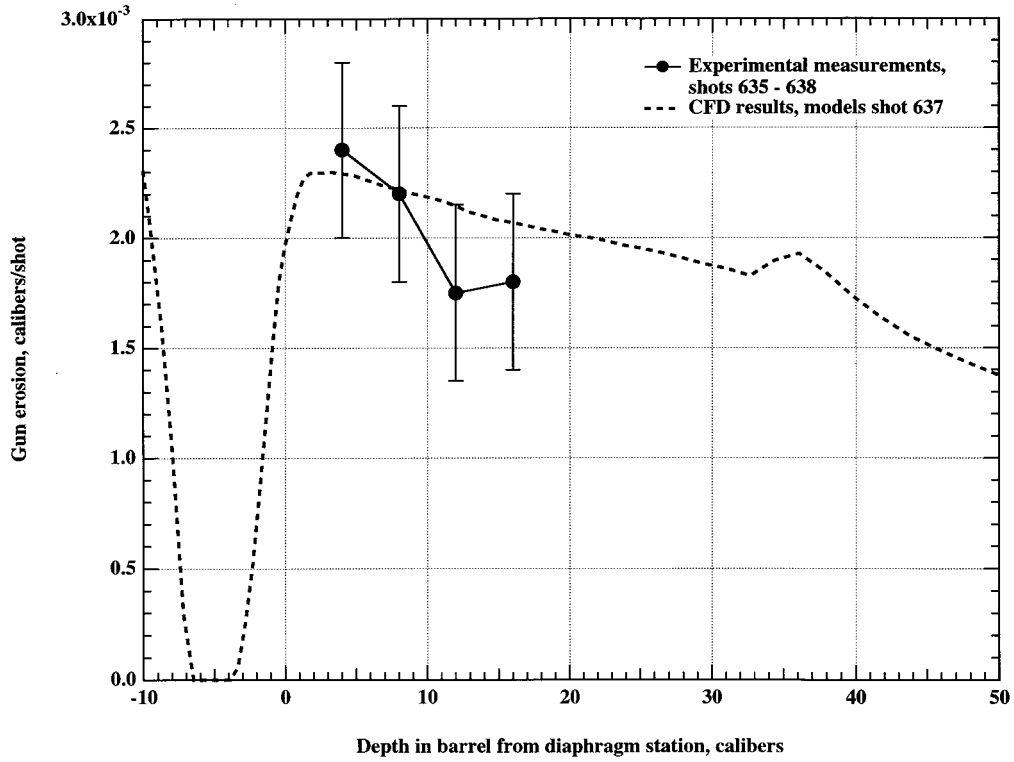

Figure 7. Experimental and numerical gun erosion values for Ames 0.5" gun for four shots in data block 3.

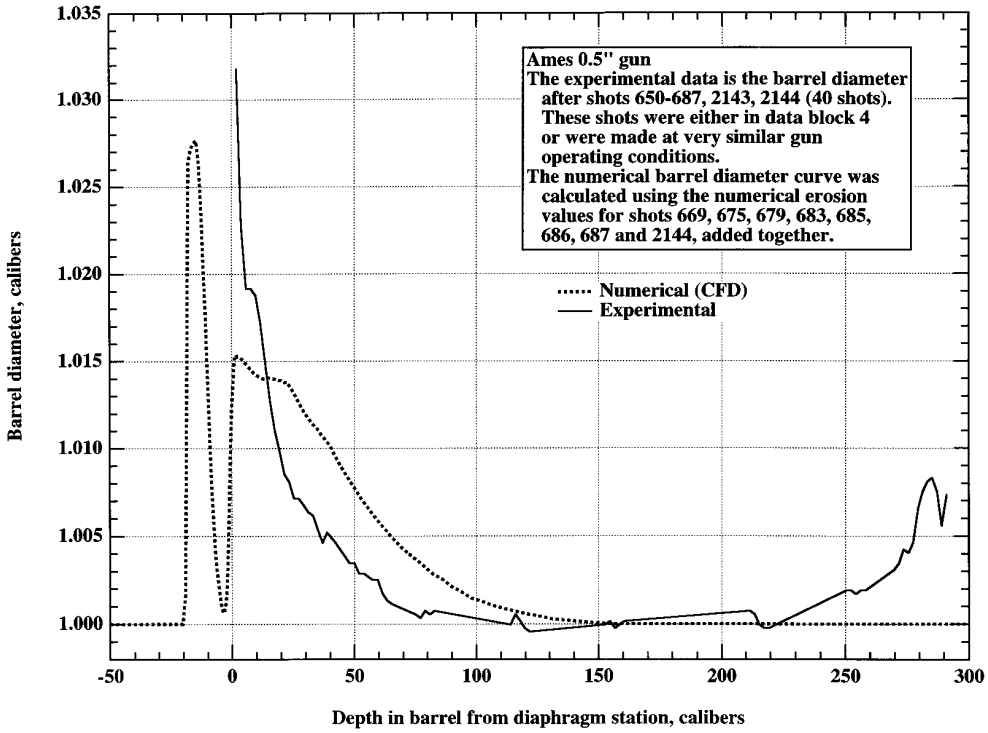

Figure 8. Experimental and numerical gun erosion values for Ames 0.5" gun for 40 shots in data block 4 or under similar gun operating conditions.

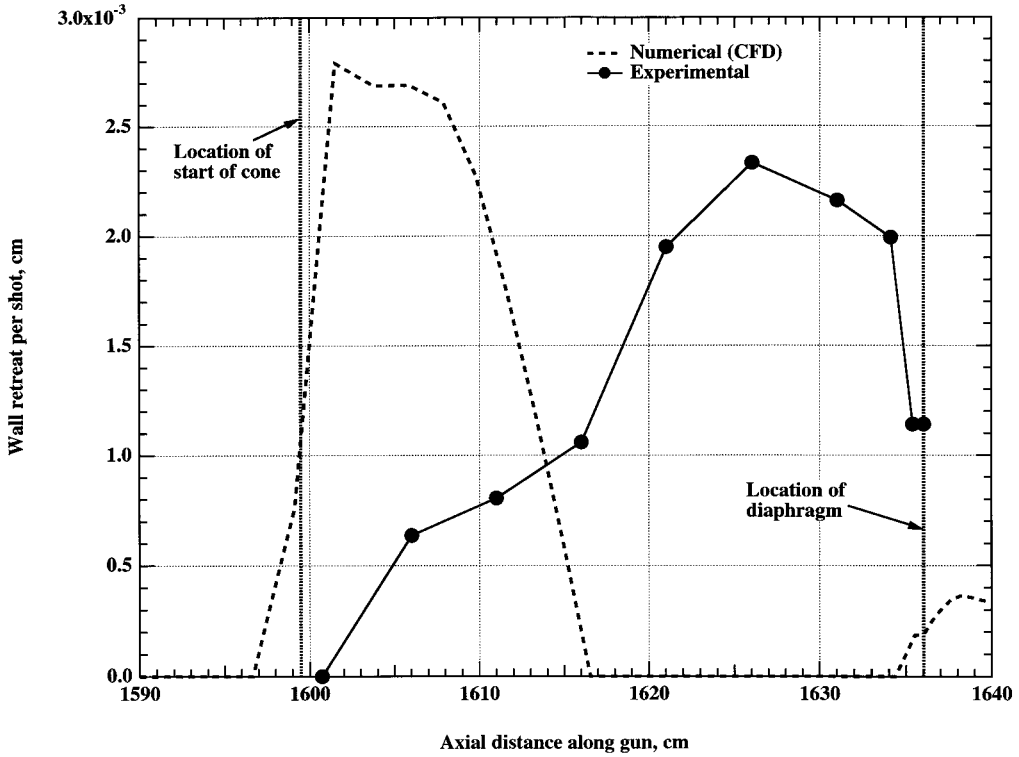

Figure 9. Experimental and numerical erosion for 8.1 degree contraction cone for Ames 0.5" gun. See text for discussion of gun operating conditions.

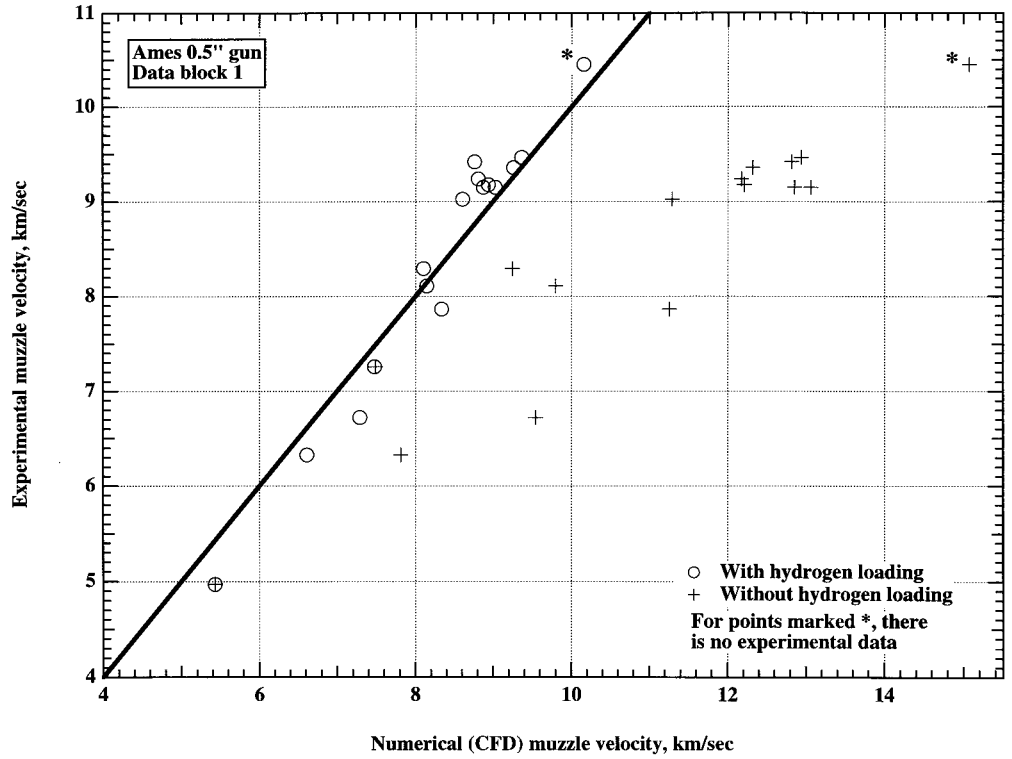

Figure 10. Experimental and numerical muzzle velocities for Ames 0.5" gun for data block 1.

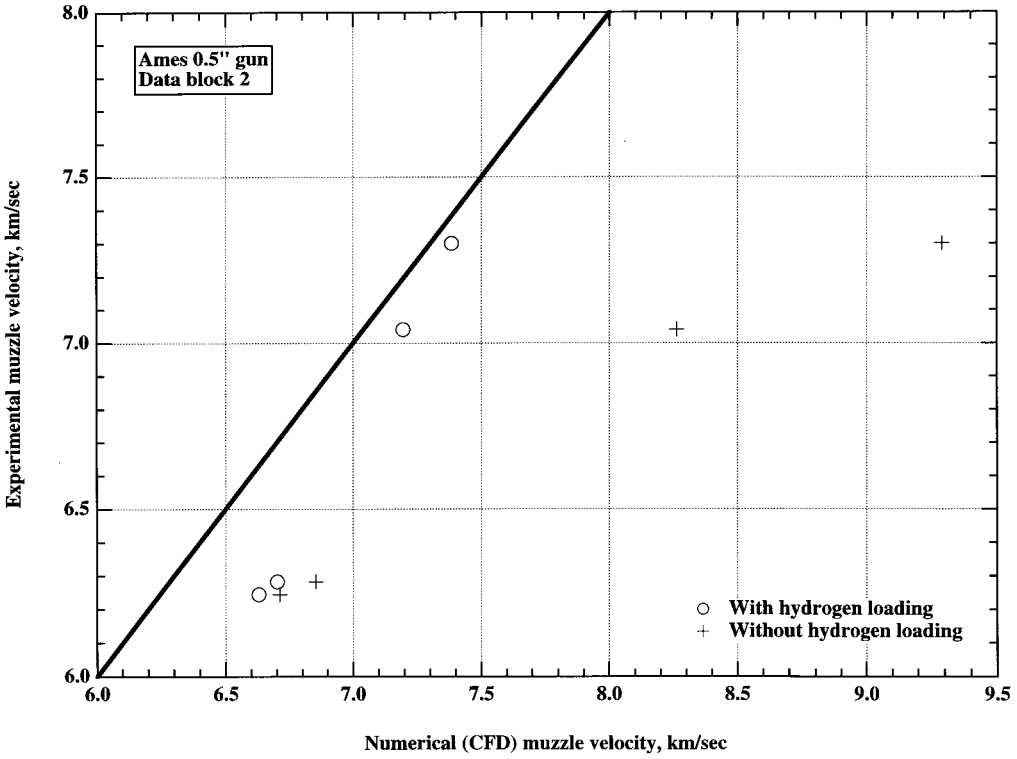

Figure 11. Experimental and numerical muzzle velocities for Ames 0.5" gun for data block 2.

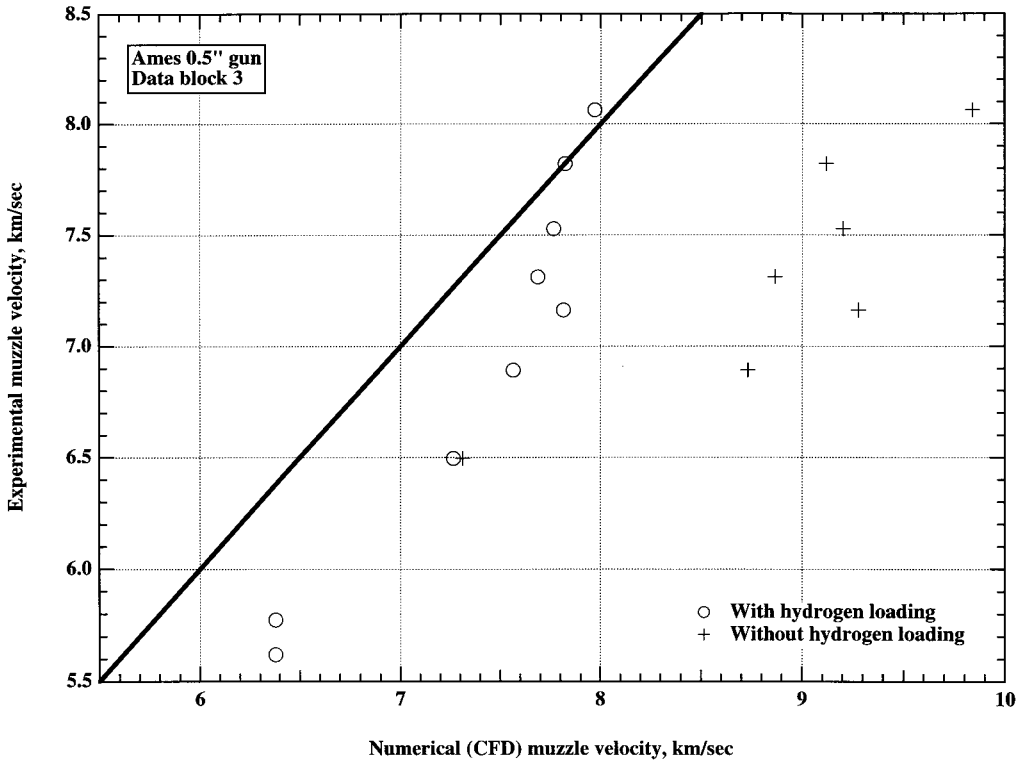

Figure 12. Experimental and numerical muzzle velocities for Ames 0.5" gun for data block 3.

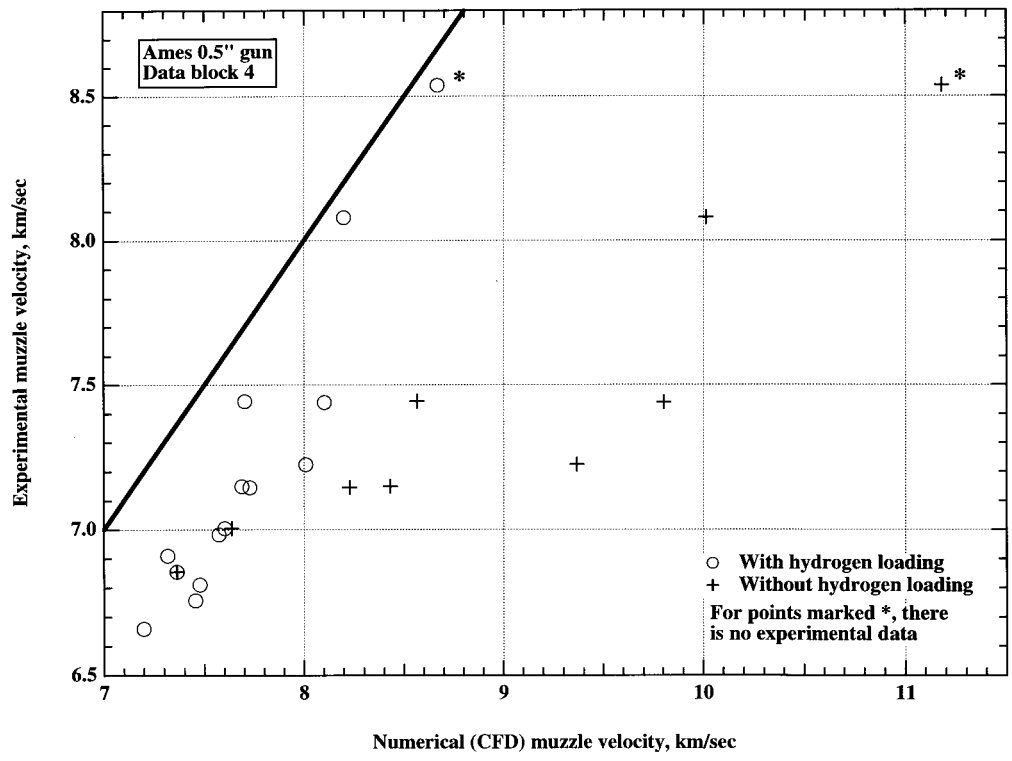

Figure 13. Experimental and numerical muzzle velocities for Ames 0.5" gun for data block 4.

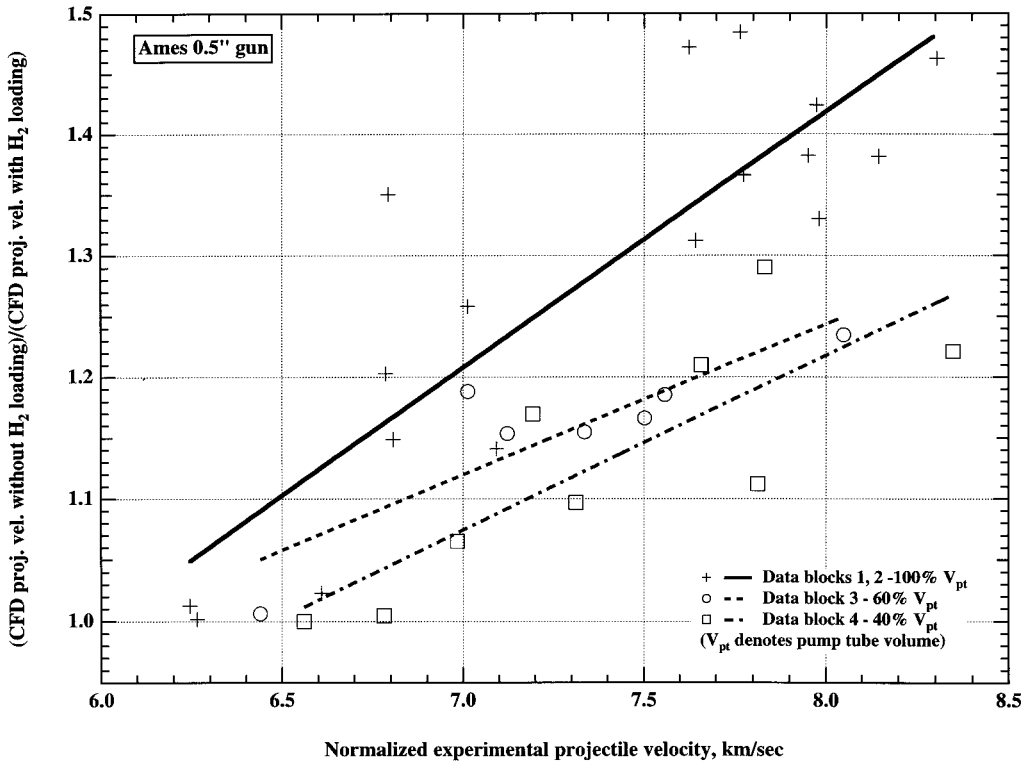

Figure 14. Ratios of CFD projectile velocities without and with hydrogen loading plotted versus normalized muzzle velocity.

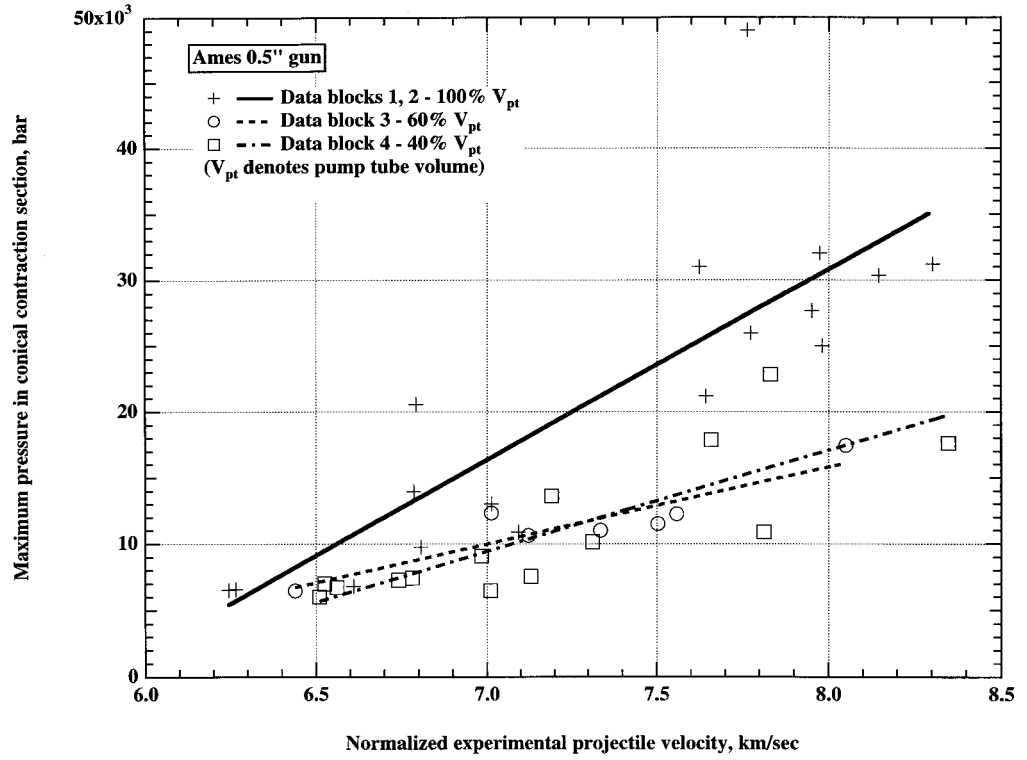

Figure 15. Calculated maximum pressures in contraction cone versus normalized experimental muzzle velocities.

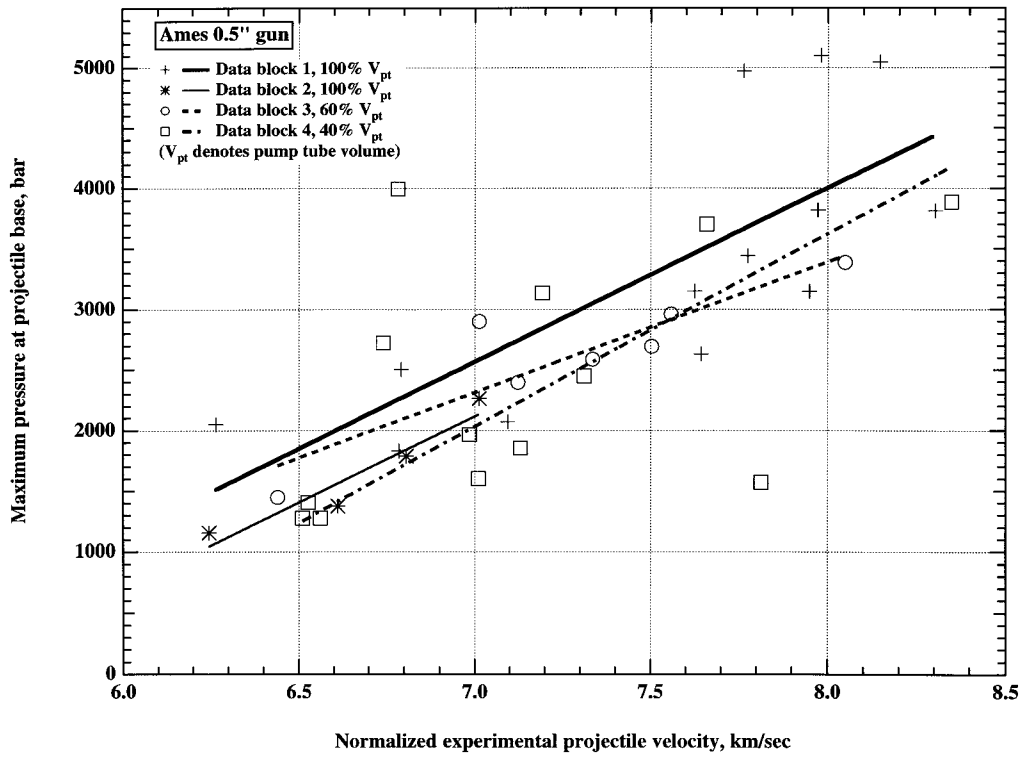

Figure 16. Calculated maximum pressures at projectile base versus normalized experimental muzzle velocities.

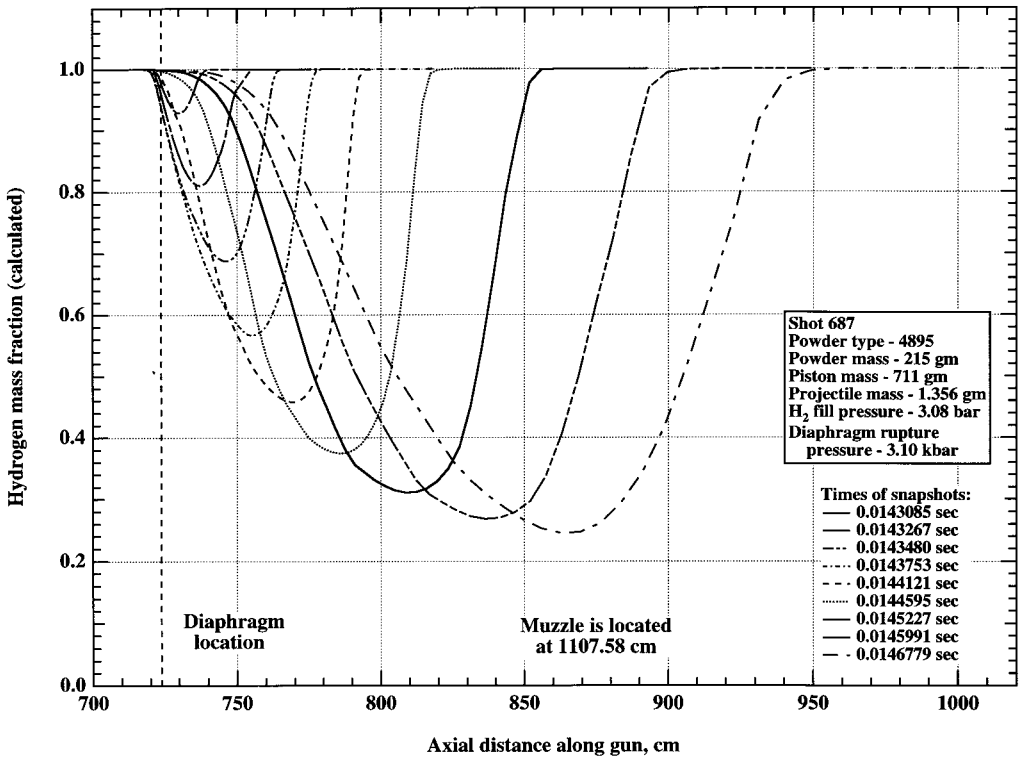

Figure 17. Calculated hydrogen mass fractions for shot 687.

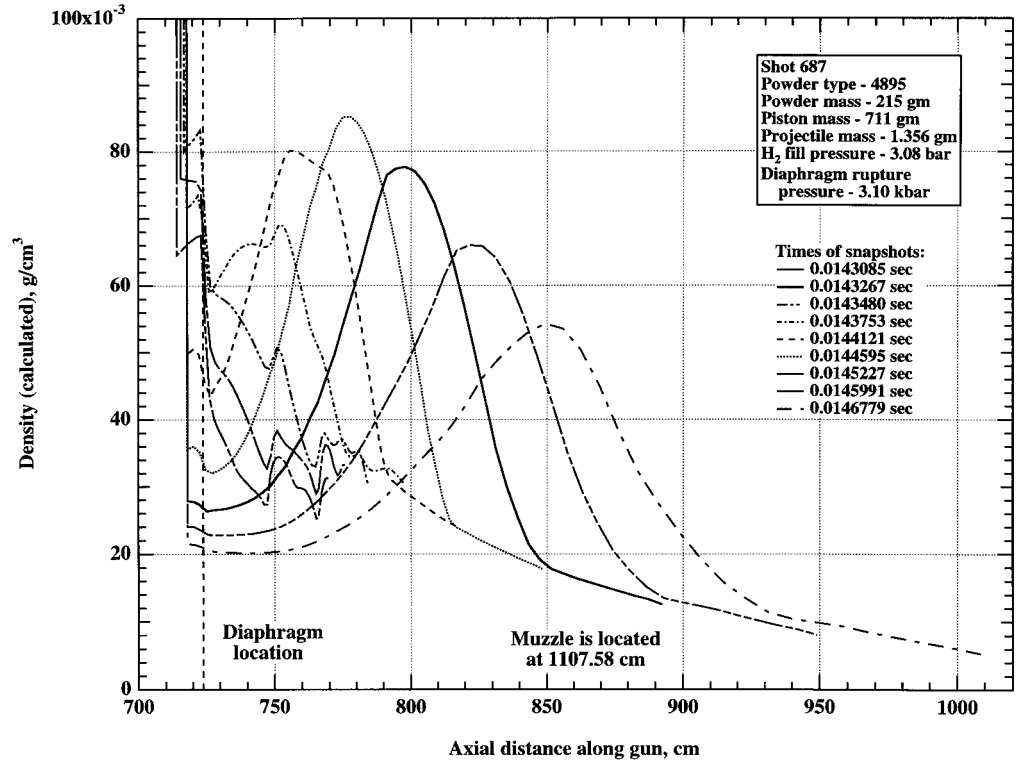

Figure 18. Calculated densities for shot 687.

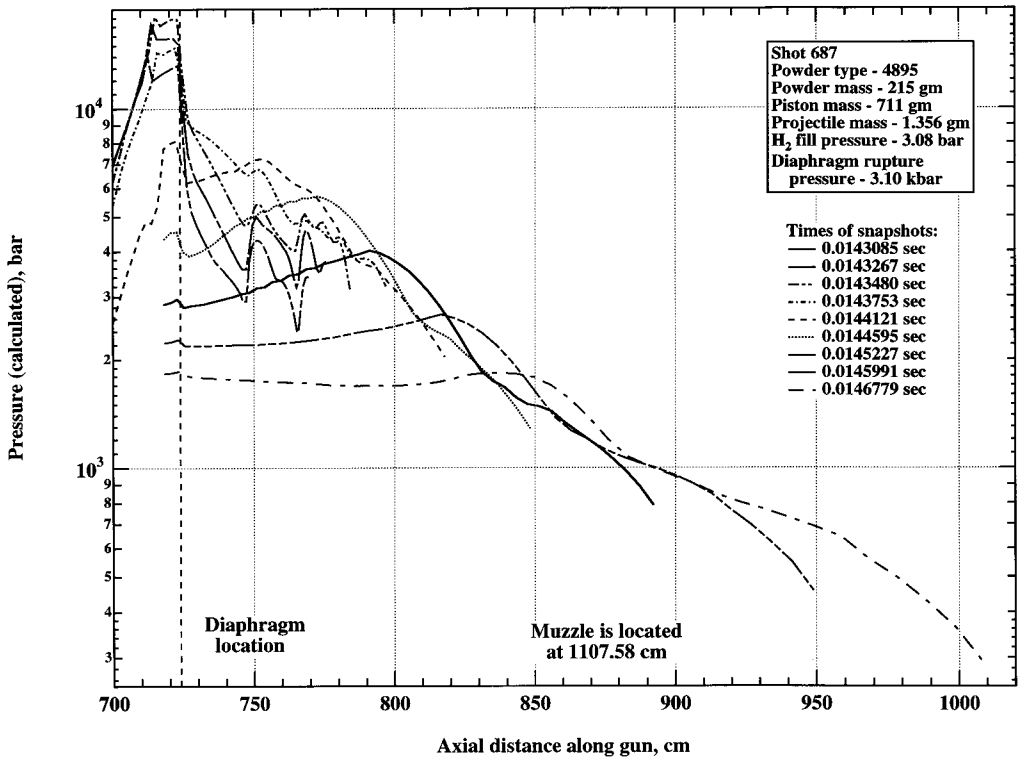

Figure 19. Calculated pressures for shot 687.

REPORT DOCUMENTATION PAGE

Form Approved
OMB No. 0704-0188

1. AGENCY USE ONLY *(Leave blank)*

2. REPORT DATE
August 1998

3. REPORT TYPE AND DATES COVERED
Technical Memorandum

4. TITLE AND SUBTITLE
CFD Modelling of Bore Erosion in Two-Stage Light Gas Guns

5. FUNDING NUMBERS
242-80-01

6. AUTHOR(S)
D. W. Bogdanoff

7. PERFORMING ORGANIZATION NAME(S) AND ADDRESS(ES)
Thermosciences Institute
Ames Research Center
Moffett Field, CA 94035-1000

8. PERFORMING ORGANIZATION REPORT NUMBER
A-9811886

9. SPONSORING/MONITORING AGENCY NAME(S) AND ADDRESS(ES)
National Aeronautics and Space Administration
Washington, DC 20546-0001

10. SPONSORING/MONITORING AGENCY REPORT NUMBER
NASA/TM–1998-112236

11. SUPPLEMENTARY NOTES
Point of Contact: D. W. Bogdanoff, Ames Research Center, MS 230-2, Moffett Field, CA 94035-1000
(650) 604-6138

12a. DISTRIBUTION/AVAILABILITY STATEMENT
Unclassified — Unlimited
Subject Category 14 Distribution: Standard
Availability: NASA CASI (301) 621-0390

12b. DISTRIBUTION CODE

13. ABSTRACT *(Maximum 200 words)*

A well-validated quasi-one-dimensional computational fluid dynamics (CFD) code for the analysis of the internal ballistics of two-stage light gas guns is modified to explicitly calculate the ablation of steel from the gun bore and the incorporation of the ablated wall material into the hydrogen working gas. The modified code is used to model 45 shots made with the NASA Ames 0.5" light gas gun over an extremely wide variety of gun operating conditions. Good agreement is found between the experimental and theoretical piston velocities (maximum errors of ±2% to ±6%) and maximum powder pressures (maximum errors of ±10% with good igniters). Overall, the agreement between the experimental and numerically calculated gun erosion values (within a factor of 2) was judged to be reasonably good, considering the complexity of the processes modelled. Experimental muzzle velocities agree very well (maximum errors of 0.5–0.7 km/sec) with theoretical muzzle velocities calculated with loading of the hydrogen gas with the ablated barrel wall material. Comparison of results for pump tube volumes of 100%, 60% and 40% of an initial benchmark value show that, at the higher muzzle velocities, operation at 40% pump tube volume produces much lower hydrogen loading and gun erosion and substantially lower maximum pressures in the gun. Large muzzle velocity gains (2.4–5.4 km/sec) are predicted upon driving the gun harder (that is, upon using higher powder loads and/or lower hydrogen fill pressures) when hydrogen loading is neglected; much smaller muzzle velocity gains (1.1–2.2 km/sec) are predicted when hydrogen loading is taken into account. These smaller predicted velocity gains agree well with those achieved in practice. CFD snapshots of the hydrogen mass fraction, density and pressure of the in-bore medium are presented for a very erosive shot.

14. SUBJECT TERMS
CFD modelling, Bore erosion, Two-stage light gas guns

15. NUMBER OF PAGES
39

16. PRICE CODE
A03

17. SECURITY CLASSIFICATION OF REPORT	18. SECURITY CLASSIFICATION OF THIS PAGE	19. SECURITY CLASSIFICATION OF ABSTRACT	20. LIMITATION OF ABSTRACT
Unclassified	Unclassified		